Luna, L. V., Bookhagen, B., Niedermann, S., Rugel, G., Scharf, A., Merchel, S. (2018): Glacial chronology and production rate cross-calibration of five cosmogenic nuclide and mineral systems from the southern Central Andean Plateau. - *Earth and Planetary Science Letters*, *500*, pp. 242—253.

DOI: http://doi.org/10.1016/j.epsl.2018.07.034

Title

Glacial chronology and production rate cross-calibration of five cosmogenic nuclide and mineral systems from the southern Central Andean Plateau

Authors and Affiliations

Lisa V. Luna[1], Bodo Bookhagen[1], Samuel Niedermann[2], Georg Rugel[3], Andreas Scharf[3], Silke Merchel[3]

[1]University of Potsdam, Institute of Earth and Environmental Science, Karl-Liebknecht-Str. 24-25, 14476 Potsdam-Golm, Germany

[2]GFZ German Research Center for Geosciences, Telegrafenberg, 14473 Potsdam, Germany

[3]Helmholtz-Zentrum Dresden-Rossendorf, Bautzner Landstraße 400, 01328 Dresden, Germany

Corresponding author: Bodo Bookhagen (bodo.bookhagen@uni-potsdam.de)

Abstract

Glacial deposits on the high-altitude, arid southern Central Andean Plateau (CAP), the Puna in northwestern Argentina, document past changes in climate, but the associated geomorphic features have rarely been directly dated. This study provides direct age control of glacial moraine deposits from the central Puna (24°S) at elevations of 3900-5000 m through surface exposure dating with cosmogenic nuclides.

Our results show that the most extensive glaciations occurred before 95 ka and an additional major advance occurred between 46 and 39 ka. The latter period is synchronous with the highest lake levels in the nearby Pozuelos basin and the Minchin (Inca Huasi) wet phase on the Altiplano in the northern CAP. No significant glacial advance was found during the Tauca wet phase (24-15 ka), suggesting that the necessary atmospheric conditions for westward moisture transport from the foreland to the central Puna Plateau did not exist during this time.

Additionally, the volcanic lithologies of the deposits allow us to establish production ratios at low latitude and high elevation for five different nuclide and mineral systems: ^{10}Be, ^{21}Ne, and ^{26}Al from quartz (11 or 12 samples) and ^{3}He and ^{21}Ne from pyroxene (10 samples). We present production ratios for all combinations of the measured nuclides and cross-calibrated production rates for ^{21}Ne in pyroxene and quartz for the high, (sub-)tropical Andes. The production rates are based on our ^{10}Be-normalized production ratios and a weighted mean of reference ^{10}Be production rates calibrated in the high, tropical Andes (4.02 ± 0.12 at g^{-1} yr^{-1}). These are, $^{21}Ne_{qtz}$: 18.1 ± 1.2 and $^{21}Ne_{px}$: 36.6 ± 1.8 (En_{88-94}) scaled to sea level and high latitude using the Lal/Stone scheme, with 1σ uncertainties. As ^{3}He and ^{26}Al have been directly calibrated in the tropical Andes, we recommend using those rates.

Finally, we compare exposure ages calculated using all measured cosmogenic nuclides from each sample, including 11 feldspar samples measured for ^{36}Cl, and a suite of previously published production rates.

Keywords

cosmogenic nuclides, production rate, cross-calibration, South American Monsoon, Quaternary Climate Change, moraine

Highlights

- The most extensive glaciations in the southern Central Andean Plateau predate 95 ka.
- A glacial advance occurred between 46 and 39 ka during the Minchin wet phase.
- No significant advance was found during the Tauca wet phase (24-15 ka).
- Production rates were cross-calibrated for five different nuclide/mineral pairs.
- Exposure ages from six nuclide/mineral pairs from the same samples were compared.

1. Introduction

The southern Central Andean Plateau (CAP) is a high-altitude, internally drained orogenic plateau between the Eastern and Western Cordilleras of the Andes in northwestern Argentina (Fig. 1, e.g., Allmendinger et al., 1997). The southern CAP is referred to as the Puna and is located to the south of the Altiplano (northern CAP). Climatically it sits within the Arid Diagonal, a zone of aridity stretching from coastal Peru in the northwest to the Argentine Pampas in the southeast. Although the Puna is a critical region in the Andean climate system (e.g., Baker and Fritz, 2015), paleoclimate data is scarce.

Records of mountain glaciations provide constraints on paleoclimatic conditions, and a growing body of work has concentrated on dating glacial features in the tropical and subtropical Andes, as well as farther south in the temperate Andes (e.g., Blard et al., 2014; Zech et al., 2009), summarized in Jomelli et al. (2014). Glacial features have been documented on the Puna, but rarely directly dated (e.g., Haselton et al., 2002). Here, we present the first glacial chronology for the central Puna, using cosmogenic nuclide based surface exposure ages from moraine boulders from two volcanic complexes (Fig. 1).

An essential input for determining exposure ages is the local production rate (e.g., Balco et al., 2008). Production rates differ for each nuclide and target mineral, and also change with time, latitude, and altitude, due to the strength and geometry of the Earth's magnetic field and the thickness of the atmosphere. Therefore, estimated production rates at the study site and the resulting exposure ages depend not only on the calibration site where the reference production rate was established, but also on the scaling method, geomagnetic field history, and atmospheric model used.

One strategy to reduce uncertainty in the production rate based on the choice of scaling model is to use a calibration site that is close to the target sampling site in distance, elevation, and time (Balco et al., 2008). However, high-quality production rate calibration sites do not yet exist for all nuclides in all parts of the world (Borchers et al., 2016). Different cosmogenic nuclides are produced at a certain ratio, which may also vary geographically to a small extent. If this ratio is known, it can be combined with a locally calibrated production rate for one nuclide to calculate production rates for other nuclides (e.g., Amidon et al., 2009; Goethals et al., 2009a). The volcanic composition of the sampled boulders allows us to determine the production ratios between five different nuclide and mineral systems: ^{10}Be, ^{26}Al, and ^{21}Ne in quartz and ^{3}He and ^{21}Ne in pyroxene.

The majority of cosmogenic nuclide exposure dating studies use only one or two nuclides, based on the lithology of the samples. When considering ages calculated at different localities with different nuclides, as is often done in review studies, it is largely assumed that these ages are directly comparable (e.g., Jomelli et al., 2014). However, this assumption has seldom been tested. Our samples and nuclide combination provide the additional possibility to directly compare exposure ages calculated from six different nuclide/mineral systems from the same samples: the five listed above and ^{36}Cl from feldspar.

In summary, our study addresses three main goals: (1) Establish the first glacial chronology for the central Puna; (2) Determine production ratios between five different cosmogenic nuclide/target mineral pairings at high elevation and low latitude; and (3) Directly compare ages calculated from each nuclide system from the same sample to test the assumption that they are equivalent.

2. Geologic, Climatic, and Geomorphologic Setting

Uplift of the CAP began between 15 and 20 Ma, with magmatism beginning during the late Oligocene (~26 Ma) (Allmendinger et al., 1997). In the late Miocene, numerous eruptions occurred along NW-SE striking transverse fault systems, producing the basaltic-andesitic to dacitic del Medio, Pocitos, and Quevar volcanoes that host the moraines we sampled. These stratovolcanoes have K-Ar and Ar-Ar ages ranging between 8 and 5 Ma (Matteini et al., 2002).

Precipitation on the CAP is dominated by summer moisture brought in through the South American Monsoon System (SAMS) (e.g., Garreaud et al., 2003). The semi-arid study area receives <500 mm yr^{-1} of precipitation, at least 70% of which falls during the austral summer between December and February (DJF) (Castino et al., 2016).

The geomorphologic shapes of the studied moraines tend to be smooth, with boulders ranging in height from several tens of centimeters up to ~2 m (Fig. 2, see Supplementary Materials for further detail). We sampled five moraines from four valleys: del Medio, Pocitos, Quirón M1 and M2, and Quevar (Fig. 3). These range in elevation from 3900 – 5000 m, with the lowest moraines occurring on the del Medio and Pocitos volcanoes and the highest on Quevar (Table 1).

Moraine sequences are best preserved in the Quirón and Pocitos valleys. At Quirón, the lowest lateral moraine (M1) displays broad and flat morphology. The M2 frontal moraine stratigraphically predates the M1 moraine and is rounded. Up-valley of the M2 moraine, complex till covers the valley floor. In the Pocitos valley, hummocky terrain covers the floor of the cirque, and some small (~2m high) moraine features occur near the valley walls. Boulder samples from these moraines did not produce dateable material. Two rounded lateral moraines characterize the lower section of the valley – the lowest of these was dated. Farther downstream, large boulders cover an alluvial fan at the mouth of the valley and may be remnants of earlier glacial advances, but have likely been re-transported.

At del Medio and Quevar, we took a similar approach of sampling the lowest lateral moraine from the respective valleys. At Quevar, we also observed large boulders farther downstream, which, similarly to Pocitos, may be related to earlier glacial advances.

3. Methods and Analytical Results

3.1 ^{10}Be and ^{26}Al in Quartz

Quartz was separated by standard mineral separation techniques. Sample purity was checked by inductively coupled plasma optical emission spectrometry (ICP-OES). Be and Al were extracted at Helmholtz-Zentrum Dresden-Rossendorf (HZDR) in Dresden, Germany following a modified version of methods described in Merchel and Herpers (1999). We added ~300 µg of in-house ^{9}Be carrier ('Phena EA', 2246 ± 11 µg g^{-1} ^{9}Be, Merchel et al., 2013a) and ~750 µg ^{27}Al carrier (Roth Al single element standard solution for ICP, 1000.5 ± 2.0 µg ml^{-1} ^{27}Al; density = 1.011 g cm^{-3}) to the pure quartz samples before dissolution. The total Al concentration in the sample was measured from an aliquot taken after dissolution by ICP-OES at the University of Potsdam.

Be and Al isotope ratios were measured by accelerator mass spectrometry (AMS) at the DREAMS facility at HZDR (Rugel et al., 2016). ^{10}Be/^{9}Be ratios were normalized to in-house standard SMD-Be-12 (Akhmadaliev et al., 2013), which has been cross-calibrated to the NIST SRM 4325 standard (^{10}Be/^{9}Be ratio of 2.79 ± 0.03 x 10^{-11}) (Nishiizumi et al., 2007). Al ratios were normalized to SMD-Al-11 (Rugel et al., 2016), which is traceable to primary standards (see Supplementary Text for details). Measured ^{10}Be/^{9}Be ratios for the samples range from 3.40 x 10^{-13} to 2.47 x 10^{-12}, with a mean analytical uncertainty of 2.2% (1σ, n=11), excluding one outlier where most of the sample was lost during chemical processing (Table A1). Measured ^{26}Al/^{27}Al ratios range from 1.01 x 10^{-12} to 1.43 x 10^{-11}, with a mean analytical uncertainty of 2.5% (1σ, n=11), excluding the same outlier (Table A1). Higher uncertainties on the ^{26}Al concentrations result from propagating an estimated 3% uncertainty on the total ^{27}Al ICP-OES measurements. Blank corrections for ^{10}Be were between 0.3 and 1.4% and for ^{26}Al between 0.04 and 0.20%.

3.2 ^{36}Cl in Feldspar

Feldspar was separated from whole rock samples through magnetic separation and froth floatation. ^{36}Cl extraction chemistry was performed in the ^{36}Cl laboratory at HZDR following Merchel et al. (2013b). After rinsing overnight with deionized water and dissolving ~20% of the sample in an HF/HNO_3 solution, a solid aliquot of the grains was taken to determine the chemical composition of the feldspar. About 1.5 mg of carrier enriched in ^{35}Cl ($^{35}Cl/^{37}Cl = 999$) was then added to the samples before dissolution and Cl extraction.

Cl isotope ratios were measured by AMS at the DREAMS facility at HZDR. $^{36}Cl/^{35}Cl$ ratios were normalized to the primary-type SM-Cl-12 standard (Merchel et al., 2011). Measured $^{36}Cl/^{35}Cl$ ratios ranged from 4.19×10^{-13} to 2.00×10^{-12} with a mean analytical uncertainty of 2.3% (1σ, $n = 11$) (Table A2). Blank corrections ranged from 0.5 to 1.4%. The natural Cl content in the feldspars was determined by isotope dilution AMS.

To determine composition dependent ^{36}Cl production rates, Ca, K, Ti, and Fe were measured from the feldspar separates by ICP-OES at the University of Potsdam (Table A3). Major and minor elements from the whole rock were measured by X-ray fluorescence (XRF) at the German Research Center for Geosciences (GFZ) in Potsdam, with the exceptions of U, Th, Li, Gd, and Sm, which were measured by inductively coupled plasma mass spectrometry (ICP-MS), Cl, which was measured by ion chromatography, and H_2O and CO_2, which were measured by gas chromatography. Boron was measured by prompt gamma activation analysis (PGAA) at the Heinz Maier-Leibnitz Zentrum in Garching, Germany (Table A4). Whole rock density was determined using a pycnometer (Table 1).

3.3 ^{21}Ne in Quartz

^{20}Ne, ^{21}Ne, and ^{22}Ne from the quartz separates were measured by noble gas mass spectrometry at GFZ following Niedermann et al. (1997). Gases were extracted from the samples by stepwise heating at 400°C, 800°C, and 1200°C in a resistance heated furnace and He and Ne were admitted separately into the VG5400 noble gas mass spectrometer. Blank measurements had an atmospheric composition and ranged from $0.9 – 1.4 \times 10^{-12}$ cm^3 STP (Standard Temperature and Pressure) for ^{20}Ne depending on temperature. Aliquots from three samples were crushed in vacuo to determine the isotopic composition of trapped Ne in the crystals.

Total ^{21}Ne excesses were calculated using combined data from the 400°C and 800°C steps (Niedermann, 2002) and the following equation:

Equation 1

where ex = excess, m = measured, and tr = trapped, and assuming that $^{20}\mathrm{Ne}_{ex}$ can be ignored (Niedermann, 2002). $(^{21}\mathrm{Ne}/^{20}\mathrm{Ne})_{tr}$ was taken to be 0.00304 ± 0.00013, the error weighted mean of the crushing measurements. Two samples of the CREU-1 quartz standard gave ^{21}Ne excess values (relative to atmospheric trapped Ne) of 348.2 ± 7.4 (1σ) x 10^6 at g^{-1} and 347.5 ± 6.9 (1σ) x 10^6 at g^{-1}, in perfect agreement with the CREU-1 reference value of 348 ± 5 (1σ) x 10^6 at g^{-1} (Vermeesch et al., 2015).

Measured $^{21}\mathrm{Ne}/^{20}\mathrm{Ne}$ and $^{22}\mathrm{Ne}/^{20}\mathrm{Ne}$ ratios plot very near to the spallation line representing a two-component mix between cosmogenic and atmospheric components (Fig. A1). Cosmogenic ^{21}Ne excesses range from 8.50 ± 0.28 (1σ) to 66.9 ± 1.3 (1σ) x 10^6 at g^{-1}, with a mean analytical error of 2.7% (n = 11, 1σ), which is dominated by the uncertainty of the mass spectrometer sensitivity (Table A5).

3.4 ^{3}He and ^{21}Ne in Pyroxene

He and Ne concentrations and isotope compositions in pyroxene were measured at GFZ. Pyroxene was separated from whole rock samples through crushing, sieving to 125-500 μm, magnetic separation, heavy liquid separation, and finally by acid leaching inspired by Bromley et al. (2014). Samples were leached for 4-6 hours in a 1% HF/1% HNO_3 solution in an ultrasonic bath, then checked for purity with a binocular microscope. If still substantially impure, samples were leached one or two additional times. After leaching, samples were hand-picked.

Pyroxene separates were manually crushed under vacuum to determine the trapped $^3\mathrm{He}/^4\mathrm{He}$ and $^{21}\mathrm{Ne}/^{20}\mathrm{Ne}$ ratios. After crushing, samples were sieved to >100 μm before heating in order to minimize the contribution of atmospheric He irreversibly adsorbed to the grains (Protin et al., 2016). However, stepwise heating measurements of both the >100 μm and <100 μm fractions of LL030215-03A after crushing yielded identical ^{3}He concentrations (Table A6), suggesting that there was no contribution of atmospheric He.

After baking at 100°C for one week, noble gases were extracted in two heating steps at 900 and 1750°C, purified, and measured in a Helix SFT mass spectrometer using procedures similar to those for quartz samples. During the Ne measurements, severe ‘memory effects’ were observed, a phenomenon where some gas ions from the current sample are lost through implantation into the mass spectrometer walls, and some previously implanted ions are released. As a result, the original isotopic ratios rapidly changed and tended toward atmospheric ratios over the course of the measurement. In order to calculate the true sample ratios, the ‘memory effect’ was corrected for following Goethals et al. (2009b), and the uncertainty of the correction was included in the total uncertainty. As argued by Goethals et al. (2009b), any inaccuracy arising from the memory correction would only affect the ^{22}Ne/^{20}Ne ratio (and thus the position of data in the three-isotope plot, cf. Fig. A1), but not the ^{21}Ne/^{20}Ne ratio or the ^{21}Ne excess.

The ^{3}He/^{4}He ratio determined by crushing varies widely between samples, ranging from 0.33 x 10^{-6} to 80 x 10^{-6}, the latter value being unrealistically high for magmatic He and suggesting that some cosmogenic ^{3}He was released during crushing, though in abundances that are negligible compared to those released by heating. For stepwise heating measurements, blank values for ^{4}He ranged from 5 x 10^{-12} to 1 x 10^{-10} cm^{3} STP. Blank corrected total measured ^{3}He ranged from 64.8 – 622 x 10^{6} at g^{-1}, with a mean uncertainty of 1.8% (n = 10, 1σ) (Table A6). Two aliquots of the CRONUS-P pyroxene standard material were measured alongside the samples and gave ^{3}He concentrations of 4.86 ± 0.10 x 10^{9} and 4.79 ± 0.10 x 10^{9} at g^{-1}, which agree within 2σ uncertainties with the global mean value of 5.02 ± 0.12 x 10^{9} at g^{-1} (Blard et al., 2015).

^{21}Ne$_{px}$ excesses were calculated using Eq. 1 and assuming an atmospheric ratio for trapped Ne. In many cases, ^{20}Ne concentrations were barely above blank level, which would lead to a large uncertainty from a blank correction. However, assuming that both the trapped and blank gases have atmospheric composition, the blank correction does not need to be known and will not affect the ^{21}Ne excess. ^{21}Ne/^{20}Ne and ^{22}Ne/^{20}Ne ratios for both the sample and CRONUS-P measurements plot very close to the spallation line (Fig. A1). ^{21}Ne excesses ranged from 17.70 to 126.8 x 10^{6} at g^{-1}, with a mean uncertainty of 2.4% (n = 10, 1σ) (Table A6).

U, Th, and Li concentrations from the pyroxene crystals were determined by ICP-MS and major/minor elements were determined by ICP-OES, both at GFZ (Table A3).

3.4.1 Estimating Cosmogenic ^{3}He Concentrations

The total measured ^{3}He in a pyroxene sample stems from three sources: trapped ^{3}He, nucleogenic and cosmogenic thermal neutron produced ^{3}He, and spallation produced cosmogenic ^{3}He. The total measured ^{4}He in a sample is a combination of trapped ^{4}He and radiogenic ^{4}He (e.g., Niedermann, 2002). The contributions of these sources were estimated following Blard and Farley (2008); see Supplementary Text for complete equations and further detail.

In brief, radiogenic ^{4}He (^{4}He*) produced by decay of U and Th was calculated following Blard and Farley (2008) (see Supplementary Text for details). Since the U and Th concentrations in the rock matrix are in some cases up to 650 times higher than those in the pyroxene crystals, ^{4}He* implanted from the matrix is the dominant source of ^{4}He* in these pyroxene samples. Assuming a closure age for He of 8 Ma (Matteini et al., 2002), the calculated ^{4}He* concentrations turn out higher than the total measured ^{4}He concentrations for all samples except one (Table A7). The discrepancy between the calculated and measured concentrations is most likely explained by loss of material from the surface of the crystals, where implanted ^{4}He* is concentrated, through leaching.

Nevertheless, the consistently higher predicted values with respect to the measured ones suggest that the majority of ^{4}He in these samples is radiogenic. Furthermore, the concentrations of ^{4}He released by heating were often two orders of magnitude higher than those released by crushing, which is typical of samples dominated by radiogenic ^{4}He. The $^{4}He_{tr}$ component is likely to be very small when compared with the total measured ^{4}He. It then follows that the concentration of trapped ^{3}He is also small with respect to the total measured ^{3}He. As the trapped ^{3}He concentrations are similar to the analytical uncertainty of the total measured ^{3}He concentrations, and far less than uncertainties of the resulting ages, we apply no corrections for trapped ^{3}He and assume that all measured ^{3}He is either cosmogenic or nucleogenic in origin. Doing so should have a negligible effect on the resulting production ratio or age calculations.

^{3}He produced by thermal neutron absorption by ^{6}Li was corrected for following Andrews et al. (1986). Lithium concentrations in the pyroxene samples range from 24-71 μg g^{-1}. For the contribution from cosmogenic thermal neutrons, an erosion rate of 1 mm kyr^{-1} and the ^{10}Be or $^{21}Ne_{px}$ exposure age of the sample was used (Table A7).

After corrections, the concentrations of cosmogenic spallation produced ^{3}He range from 60-574 x 10^{6} at g^{-1}, which is 87-94% of the measured ^{3}He (Table A7).

3.5 Production Rates and Age Calculations

Using CRONUScalc Matlab codes (Marrero et al., 2016), we calculated exposure ages from all measured nuclide systems using previously published production rates to test the hypothesis that ages from the same samples are directly comparable. ^{21}Ne ages from pyroxene were calculated using a modified version of the ^{21}Ne from quartz functions. We used the time-dependent Lal/Stone (Lm) scaling model, with the default CRONUScalc v2.0 geomagnetic history, and estimated atmospheric pressure from the ERA-40 dataset (see references in Marrero et al., 2016). The attenuation length for spallation reactions was taken to be 160 g cm^{-2} (e.g., Balco et al., 2008).

Where available, we took production rates from nearby calibration sites in order to minimize the influence of the scaling and atmospheric models. For ^{3}He, we used the weighted mean of two production rates calibrated within 500 km of our study site at the Tunupa Volcano on the Altiplano Plateau and the San Pedro Volcano in the Atacama desert (Fig 1): 130.0 ± 6.3 at g^{-1} yr^{-1} SLHL (Blard et al., 2013; Delunel et al., 2016). For ^{10}Be, we used a tropical Andes regional production rate similar to that proposed by Martin et al. (2015) of 4.02 ± 0.12 at g^{-1} yr^{-1} SLHL, which is a combination of two independent ^{10}Be calibrations at the Azanques and Quelccaya sites (Kelly et al., 2015; Martin et al., 2015). The ^{3}He and ^{10}Be reference production rates were scaled to SLHL using the CREp website (http://crep.crpg.cnrs-nancy.fr, accessed Mar 04, 2016) with identical parameters as the CRONUScalc calculations (Martin et al., 2016). We combined the ^{10}Be production rate with the ^{10}Be/^{21}Ne production ratio in quartz of 0.232 ± 0.009 determined by Goethals et al. (2009a) for a ^{21}Ne production rate in quartz of 17.33 ± 0.85 at g^{-1} yr^{-1} SLHL. Similarly, we combined the ^{10}Be production rate with the ^{26}Al/^{10}Be ratio determined at the Quelccaya site in Peru (Phillips et al., 2016) of 6.74 ± 0.34, yielding a ^{26}Al production rate of 27.1 ± 1.6 at g^{-1} yr^{-1} SLHL. As there is no local calibration for ^{36}Cl in Ca-rich minerals, we used CRONUS-Earth global reference production rates, which are 51.7 ± 4.9 at (g Ca)$^{-1}$ yr^{-1} and 151 ± 14 at (g K)$^{-1}$ yr^{-1} SLHL (Borchers et al., 2016).

For ^{21}Ne in pyroxene, we calculated composition dependent production rates for each sample following Fenton et al. (2009). Reference production rates for each element were determined by normalizing model predicted ^{21}Ne production rates (Masarik, 2002) to a reference SLHL production rate of 46 ± 4 at g^{-1} yr^{-1} in olivine Fo_{81}, as found by Poreda and Cerling (1992) and rescaled using Lal/Stone time dependent scaling (Lm).

The pyroxene samples in this study are low calcium pyroxenes (En_{88-94}), with an average composition of $(Ca_{0.6},Mg_{1.74},Fe_{0.09},Ti_{0.01},Mn_{0.01})(Si_{1.90},Al_{0.11})O_3$, which means that they have a higher Mg and a lower Ca content than pyroxenes used in previous calibrations of cosmogenic ^{21}Ne production rates (e.g., Fenton et al., 2009; Amidon et al., 2009). The calculated composition dependent production rates for $^{21}Ne_{px}$ range from 31.9 – 35.1 at g^{-1} yr^{-1} SLHL. As production rates of ^{21}Ne from Mg spallation are much higher than from Ca spallation, ^{21}Ne production rates in these samples are expected to be higher than those determined in previous studies (Masarik, 2002; Fenton et al., 2009; Amidon et al., 2009).

3.5.1 Erosion Considerations

Field evidence indicated that the boulders have experienced some amount of aeolian erosion. Elsewhere on the Puna, aeolian erosion rates have been found to range between 1 and 10 mm kyr^{-1} (Bookhagen and Strecker, 2014). The highest rates were observed in unsheltered areas at ridge crests, whereas the boulder samples in this study are from relatively sheltered mountain valley bottoms. Kelly et al. (2015) found erosion rates between 1 and 5 mm kyr^{-1} for moraine boulders sampled in the Peruvian Andes, which are likely to be higher than on the Puna. These rates can unfortunately not be estimated by simultaneously solving for an exposure age and erosion rate using multiple nuclides, as the analytical uncertainty of the ratio between the nuclides in most cases overlaps a wide range of possible erosion rate and exposure age combinations (Fig. A2). We therefore consider 5 mm kyr^{-1} to be a maximum possible erosion rate, with 1 mm kyr^{-1} as a more likely estimate (see 4.1 for discussion).

3.6 Production Ratio Calculations

For the production ratio calculations, decay corrections for radioactive nuclides were made using the ^{10}Be exposure age and assuming an erosion rate of 1 mm kyr^{-1} (see S3 of the Supplementary Text for details). Although ^{36}Cl was measured from feldspar for many of these samples, we do not calculate production ratios using ^{36}Cl because the high concentrations of both Ca and K in these feldspars make it difficult to attribute production to one element or the other without making further assumptions about the production rates.

4. Exposure Age Results and Discussion

4.1 Impact of Assumed Erosion Rate on Exposure Ages and Production Ratios

The exposure ages and production ratios presented here were calculated assuming an erosion rate of 1 mm kyr^{-1} integrated over the entire time of exposure. In reality, it is unlikely that erosion rates were steady over the entire exposure period, and more likely changed with changes in climate. Unfortunately, it is difficult to reconstruct a record of erosion rates through time. Uncertainty in the erosion rate estimates affects older boulder ages more than younger ones. For samples with ^{10}Be exposure ages near 40 ka, as is the case for the Quevar and Quirón M2 moraine boulders, using a 5 mm kyr^{-1} erosion rate instead of a 1 mm kyr^{-1} rate makes the ages around 15% older (6 kyr). However, for boulders with a ^{10}Be exposure age of 95 ka, the ages become 60%, or 50 kyr, older. The oldest boulders reach steady-state conditions with respect to ^{10}Be. Thus, uncertainty on erosion rate estimates does not change the paleoclimatic interpretations for the younger moraines (40 ka), but may have an impact on the older exposure ages.

Production ratios are much less sensitive to changes in erosion rate than exposure ages. For ^{10}Be/^{21}Ne$_{qtz}$, for example, for samples with ^{10}Be exposure ages of around 40 ka, using an erosion rate of 5 mm kyr^{-1} instead of 1 mm kyr^{-1} results in an increase in the production ratio of 0.09%. For samples with exposure ages of around 90 ka, this increases only to 0.7%. As this is smaller than the analytical uncertainty, we can conclude that uncertainty in the erosion rate is not a major source of uncertainty in the production ratio determination. We do note, however, that for some nuclide pairs involving one stable and one radioactive nuclide, the production ratio shows a slight correlation with exposure age (Fig. 4).

4.2 Moraine Ages

Exposure ages were calculated for a total of 15 boulders from five moraines and one bedrock sample (Fig. 3, Table 3). We consider the ^{10}Be ages to be the most reliable, as the production rate is well constrained in the tropical Andes and the production mechanisms for ^{10}Be are relatively simple. Where ^{10}Be was not measured, we use the ^{3}He age. The samples for which radioactive nuclides were measured show no evidence of pre-exposure and burial (Figure A2).

The Quevar and Quirón M2 moraines have similar boulder exposure ages clustering between 39 and 46 ka, with one outlying older age of ~76 ka on the Quirón M2 moraine (Fig. 3). We reject this age because the particularly angular boulder likely represents a pre-exposed fallen block from which little material was eroded during transport.

The glaciers in the valleys where we sampled moraines were likely small, and thus of limited erosive power. In such a setting, it is more likely that pre-exposure influences the distribution of boulder ages than in valleys with large glaciers. Indeed, other studies of glacier chronologies from the Andes have found widely scattered boulder ages, and concluded that pre-exposure influenced the distribution (Blard et al., 2014 and references therein).

The boulder ages for the Quirón M2 and M1 moraines agree with the stratigraphic order of the moraines. Notably, the ages of the boulders from the M1 moraine increase with distance down-valley from the top of the moraine from 97 to 392 ka. The character of the moraine also changes down-valley: from boulders with many large cobbles at the higher end to boulders with small cobbles and pebbles at the lower end, suggesting that the lower end has been weathered over a longer time period. Combining this qualitative evidence with the surface exposure ages, we suggest that the moraine does not represent a single depositional event, but was likely reoccupied several times over its history. However, without additional analysis, for example geophysical observation of internal moraine structure, it is impossible to tell if each boulder represents a separate event, or whether boulders were re-transported or turned during subsequent events. We thus refrain from assigning an age to each advance. We argue that there were likely several glacial advances between 97 and 392 kyr, but cannot resolve the exact timing when they occurred.

The single bedrock sample at the Quirón site gives an exposure age of 96 ka, in good agreement with the youngest age of the Quirón M1 moraine. The sample is from a ridge 85 m of elevation higher than the highest sample. This may suggest that the bedrock was significantly eroded during one of the M1 depositional episodes, and exposed when the glacier retreated. It then follows that the ice was not as thick during the advance that created the M2 moraine.

The boulder ages on the del Medio (175 – 800 ka) and Pocitos (44.1 – 498 ka) moraines scatter too much to assign a depositional age and the sampling density is too low to identify outliers. However, the data still provide some useful information. The good agreement between the younger age on the Pocitos moraine of 44.1 ka and the Quirón M2 and Quevar moraines (39 – 46 ka) allows us to cautiously suggest that this moraine formed at a similar time. If that is the case, the other boulder age of 498 ka confirms that pre-exposure impacts the distribution of exposure ages in this area. This is further supported by the co-occurrence of exposure ages of 175 and 800 ka on the del Medio moraine.

4.3 Comparison of Moraine Ages with Regional Climate Proxies

Glaciers on the Puna are thought to be aridity limited, i.e. glacier formation is more dependent on changes in precipitation than on changes in temperature (e.g., Haselton et al., 2002). Currently, the snow line increases westward across the Puna from the Eastern Cordillera to the Western Cordillera in Chile, following the trend in aridity as easterly moisture is blocked by successive ranges (Haselton et al., 2002). Previous studies have linked periods of increased moisture with glaciations on the northern CAP (Altiplano) (e.g., Blard et al., 2014; Fritz et al., 2007), and it is likely that glaciations on the Puna also indicate periods of increased precipitation.

Very little paleoclimate data exists for the Puna, whereas the Altiplano has been more widely studied. Regional paleoclimate records include sedimentary records from the Salar de

Uyuni (Baker et al., 2001; Baker and Fritz, 2015; Fritz et al., 2004; Placzek et al., 2006), and a glacial chronology from the Uturuncu volcano in the southern Altiplano (Fig. 1; Blard et al., 2014). The Lake Titicaca sedimentary record from the northern Altiplano provides a longer record, but a modern precipitation gradient exists between the wetter northern and drier southern Altiplano that also may have existed in the past (Fritz et al., 2007; Placzek et al., 2006).

The most distal moraine at the Quirón site, Quirón M1, has boulders with ages increasing downslope from 97 to 392 ka (Fig. 3). The three oldest boulders on Quirón M1 are in broad agreement with interpreted phases of increased glaciation on the northern Altiplano (Fritz et al., 2007). Between 140 and 50 ka in the Salar de Uyuni record, there were multiple short perennial lake phases (Fritz et al., 2004). Evidence for a lake-level high stand between 115 and 100 ka exists in dated shorelines around Lake Poopo (termed Ouki phase) and between 95 and 80 ka around Uyuni (termed Salinas phase) (Placzek et al., 2006). The youngest two Quirón M1 ages of 110 and 97 ka, and the bedrock age of 96 ka, likely correspond to increased regional moisture associated with the Ouki and/or Salinas wet phases. At the risk of over-interpreting single boulder ages, we can therefore broadly conclude that the depositional events that formed Quirón M1 were likely in phase with documented periods of increased moisture on the Altiplano.

In the Eastern Cordillera, at the Tres Lagunas site in the Sierra de Santa Victoria (Fig. 1), Zech et al. (2009) found boulder ages on the most distal moraine between 181 and 86 ka (ages recalculated for comparison with this study). These ages are in good agreement with the younger Quirón M1 ages. Together, they suggest that the most extensive glaciation in the Eastern Cordillera and the Puna pre-dates the documented Tauca and the Minchin wet phases and related glacial advances on the Altiplano (Fritz et al., 2004).

Figure 5 shows that boulder ages from the Quirón M2, Quevar, and Pocitos moraines ranging from 46 to 39 ka do correlate with the documented Minchin (46-36 ka, also termed Inca Huasi) wet phase on the Altiplano (Fritz et al., 2004). Glaciers were also active on the Altiplano during this time: the lowest moraine on the Uturuncu volcano in the southern Altiplano is characterized by boulders ranging from 37-65 ka, with a mode of 40 ka (Blard et al., 2014), in excellent agreement with the ages from Quirón M2 and Quevar. Sedimentological evidence from the Pozuelos Basin, just ~30 km south of the Quirón site, suggests that the basin hosted the deepest lake between 43 and 37 ka (McGlue et al., 2013). The age concordance between the boulder ages and the Pozuelos lake record provides strong evidence for a wet phase on the Puna with glacial advances between 46 and 39 ka (Fig. 5).

This is supported by observations of a wet Minchin phase that led to increased landsliding frequency (Trauth et al., 2003) and higher lake levels (Bookhagen et al., 2001) in the Eastern Cordillera just to the east of the study area.

Interestingly, we found no boulder ages corresponding to lake-level high stands on the Altiplano during the Tauca or Coipasa wet phases, dated to 24-15 ka and 13-11 ka, respectively (Baker et al., 2001). The Tauca phase produced a lake with a larger surface area than any other in the past 120 ka (Placzek et al., 2006). Moraine boulders of this age have been dated both on the Altiplano (Blard et al., 2014) and in the Eastern Cordillera (Zech et al., 2009). However, in agreement with our findings, there is no evidence for either the Tauca or the Coipasa wet phases in the Pozuelos sedimentary record (McGlue et al., 2013). An interpretation of a weaker pluvial Tauca and/or Coipasa phase is further supported by sedimentary records from the Eastern Cordillera, where no lake-level high stands have been observed between the Minchin phase and the mid Holocene (Trauth et al., 2003; Bookhagen et al., 2001). However, we did observe smaller moraine features up-valley of the moraines that we sampled. These moraines may correspond to the Tauca or Coipasa phases, but moraine size and preservation did not allow for sampling. We can conclude that neither of these phases produced as extensive of an advance as the Minchin phase or the previous glaciations.

4.4 Establishing Production Ratios

Decay and erosion corrected production ratios for each boulder are presented in Figure 4 and Table A8. Error-weighted mean production ratios from all locations (4000 – 5000 m) and the corresponding weighted standard deviations were calculated for each nuclide pair (Table 4).

For nuclide pairs involving one stable and one radioactive nuclide, the production ratio shows a correlation with exposure age for the two oldest samples (Fig. 4). This correlation is difficult to explain but is unlikely to be caused by an incorrect estimation of erosion rates (section 4.1). An alternative explanation could be diffusion of ^{3}He and ^{21}Ne over the long exposure periods of these boulders (227 and 392 ka). There is no significant correlation between exposure age and production ratio in the samples with exposure ages less than 110 ka, and we have therefore used these samples to calculate mean production ratios.

Our mean $^{3}He_{px}/^{10}Be_{qtz}$ ratio is 37.0 ± 1.1, which is higher than the previously determined mean ratio on the Altiplano of 32.4 ± 0.9 (Blard et al., 2014, updated in Martin et al., 2015), but still within the uncertainty range of individual boulders reported in that study.

The ^{10}Be/^{21}Ne$_{qtz}$ ratio of 0.222 ± 0.009 is in good agreement with the production ratio of 0.232 ± 0.009 determined by Goethals et al. (2009a) in California, and agrees within uncertainties with ratios determined above 5000 m in the Himalaya (Amidon et al., 2013). The ^{26}Al/^{10}Be ratio of 5.87 ± 0.24 is lower than the production ratio determined by Phillips et al. (2016) of 6.74 ± 0.34 at Quelccaya in Peru (see section 4.5 for further discussion).

The ^{21}Ne$_{px}$ production rates presented here are specific to low-calcium pyroxenes with similar compositions to those measured in this study (En$_{88-94}$), as ^{21}Ne is produced from spallation of both Ca and Mg (as well as Si and Al) in pyroxene. Some of the variation in the production ratios involving ^{21}Ne$_{px}$ between samples may be explained by slight differences in Mg concentrations.

4.5 Agreement of Ages between Nuclide Systems

We present exposure ages calculated using six different cosmogenic nuclide/mineral pairs in the same boulders and previously published production rates. Since we do not know the exposure ages of the boulders a priori, we compare the other ages to the ^{10}Be ages (Fig. 6).

The ^{26}Al ages are all younger than the ^{10}Be ages because the ratio of the production rates used to calculate the ages does not reflect the production ratio determined at this site. However, the ratios between the ages (which should be 1) do not scatter very much, meaning that if the ^{26}Al production rate were lowered by 12%, the ages would all overlap within uncertainties. An alternative explanation for the comparatively young ^{26}Al ages is that the total Al concentration ICP-OES measurements could have been systematically low, lowering the calculated ^{26}Al concentrations (e.g., Goethals et al., 2009a).

The ^{21}Ne$_{qtz}$ ages and the ^{10}Be ages show very good agreement, with all ages except one agreeing within 1σ uncertainties.

The ^{36}Cl and ^{10}Be ages generally agree, but the ratios between them are more widely variable than the ratios between the ^{21}Ne$_{qtz}$, ^{26}Al, and ^{10}Be ages, meaning that for some boulders, the ages differ by more than the uncertainties. This suggests that the global CRONUS-Earth production rates for ^{36}Cl are consistent with the ^{10}Be production rates calibrated in the tropical Andes, however, the complex ^{36}Cl production mechanisms and the heightened susceptibility to production below the surface may contribute to more variability between the ages when compared with ^{10}Be ages.

The ^{3}He and ^{21}Ne$_{px}$ ages are in general slightly older than the ^{10}Be ages, with the exception of one sample. This is because the ratio of the production rates used to calculate the ages differs from the production ratio determined here, most likely because the Mg concentrations in the pyroxenes used in this study are higher than those measured in the calibration studies. Such variability between ages calculated using different nuclide systems could affect the interpretations of studies that compare ages measured with different nuclide systems.

4.6 Production Rates for $^{21}Ne_{qtz}$ and $^{21}Ne_{px}$ in the High, Tropical Andes

Using the production ratios determined in this study, and the current ^{10}Be production rate for the high, tropical Andes (Kelly et al., 2015; Martin et al., 2015), we suggest production rates for ^{21}Ne$_{qtz}$ and ^{21}Ne$_{px}$. These production rates are based on time-dependent Lal/Stone scaling as implemented in CRONUScalc and the ERA-40 atmospheric reanalysis dataset. We find production rates of 18.1 ± 1.2 at g^{-1} yr^{-1} SLHL for ^{21}Ne$_{qtz}$ and 36.6 ± 1.8 at g^{-1} yr^{-1} SLHL for ^{21}Ne$_{px}$ (En$_{88-94}$). For ^{26}Al and ^{3}He, which have been directly calibrated in the tropical Andes, we recommend using those production rates (Blard et al., 2013; Delunel et al., 2016; Phillips et al., 2016).

5. Conclusions

This study had three major goals: (1) Develop a glacial chronology for the central Puna (southern Central Andean Plateau); (2) Determine production ratios between five different cosmogenic nuclide/mineral systems in the high elevation, (sub-)tropical Andes; and (3) Test the concordance of ages calculated using six different cosmogenic nuclide/mineral pairs in the same rock samples.

We found:

- The most extensive glaciations in the central Puna occurred >95 ka, long before the global LGM and the largest lake-level high stands on the Altiplano (northern Central Andean Plateau). An additional major advance occurred between 46 and 39 ka, synchronous with a lake high stand in the Pozuelos basin near our glacial moraine sampling sites, lake-level high stands in the Eastern Cordillera and the Minchin (Inca Huasi, 46-36 ka) wet phase on the Altiplano. No significant glacial advance was found during the Tauca (24-15 ka) wet phase that resulted in glacial advances on the Altiplano.

- Production ratios were determined for all possible combinations of ^{10}Be, ^{21}Ne, and ^{26}Al in quartz, and ^{3}He and ^{21}Ne in pyroxene. Ratios involving ^{3}He, ^{10}Be, ^{21}Ne$_{qtz}$, and ^{21}Ne$_{px}$ tend to have the lowest spread between samples, suggesting the best internal consistency. These production ratios will allow future studies to use local calibrations of one nuclide system to determine production rates for another.
- In order for the ages calculated from two different nuclide systems to agree with each other, it is critical that the ratio of the production rates used matches the true production ratio at the site. Even when this is the case, exposure ages from two different nuclides from the same sample may not agree, particularly when the production mechanisms are complex, as for ^{36}Cl. Therefore, some caution must be used when comparing ages calculated from different nuclide systems, particularly when small differences have large impacts on paleoclimatic interpretations.

Acknowledgements

Part of this study was supported by the StRATEGy graduate school (DFG IRTG 2018). Parts of this research were carried out at the Ion Beam Centre (IBC) at the Helmholtz-Zentrum Dresden-Rossendorf e. V., a member of the Helmholtz Association. We would like to thank the DREAMS operator team for their assistance with AMS measurements. We further thank Enzio Schnabel, Heike Rothe, Sabine Tonn, and Andrea Gottsche at GFZ, as well as Daniel Gorzawski and Antje Musiol at University of Potsdam, for help with laboratory analyses. PGAA analyses were carried out under proposal number 12247 at the Heinz-Maier Leibnitz Zentrum by Zsolt Revay. We thank Ricardo Alonso and Manfred R. Strecker for field- and logistical support and three anonymous reviewers for detailed comments that improved the manuscript.

References

Akhmadaliev, S., Heller, R., Hanf, D., Rugel, G., Merchel, S., 2013. The new 6 MV AMS-facility DREAMS at Dresden. Nucl. Instr. Meth. Phys. Res. Sect. B 294, 5–10. doi:10.1016/j.nimb.2012.01.053

Allmendinger, R.W., Jordan, T.E., Kay, S.M., Isacks, B.L., 1997. The Evolution of the Altiplano-Puna Plateau of the Central Andes. Annu. Rev. Earth Planet. Sci. 25, 139–174.

Amidon, W.H., Rood, D.H., Farley, K.A., 2009. Cosmogenic ^{3}He and ^{21}Ne production rates calibrated against ^{10}Be in minerals from the Coso volcanic field. Earth Planet. Sci. Lett. 280, 194–204. doi:10.1016/j.epsl.2009.01.031

Amidon, W.H., Bookhagen, B., Avouac, J.P., Smith, T., Rood, D., 2013. Late Pleistocene glacial advances in the western Tibet interior. Earth Planet. Sci. Lett. 381, 210–221. doi:10.1016/j.epsl.2013.08.041

Andrews, J.N., Fontes, J.C., Michelot, J.L., Elmore, D., 1986. In-situ neutron flux, ^{36}Cl production and groundwater evolution in crystalline rocks at Stripa, Sweden. Earth Planet. Sci. Lett. 77, 49–58. doi:10.1016/0012-821X(86)90131-7

Baker, P.A., Fritz, S.C., 2015. Nature and causes of Quaternary climate variation of tropical South America. Quat. Sci. Rev. 124, 31-47. doi:10.1016/j.quascirev.2015.06.011

Baker, P.A., Rigsby, C.A., Seltzer, G.O., Fritz, S.C., Lowenstein, T.K., Bacher, N.P., Veliz, C., 2001. Tropical climate changes at millennial and orbital timescales on the Bolivian Altiplano. Nature 409, 698–701. doi:10.1038/35055524

Balco, G., Stone, J.O.H., Lifton, N., Dunai, T.J., 2008. A complete and easily accessible means of calculating surface exposure ages or erosion rates from ^{10}Be and ^{26}Al measurements. Quat. Geochronol. 3, 174–195. doi: 10.1016/j.quageo.2007.12.001

Blard, P.-H., Farley, K.A., 2008. The influence of radiogenic ^{4}He on cosmogenic ^{3}He determinations in volcanic olivine and pyroxene. Earth Planet. Sci. Lett. 276, 20–29. doi:10.1016/j.epsl.2008.09.003

Blard, P.-H., Lavé, J., Sylvestre, F., Placzek, C.J., Claude, C., Galy, V., Condom, T., Tibari, B., 2013. Cosmogenic ^{3}He production rate in the high tropical Andes (3800 m, 20°S): Implications for the local last glacial maximum. Earth Planet. Sci. Lett. 377–378, 260–275. doi:10.1016/j.epsl.2013.07.006

Blard, P.-H., Lave, J., Farley, K. A., Ramirez, V., Jimenez, N., Martin, L.C.P., Charreau, J., Tibari, B., Fornari, M., 2014. Progressive glacial retreat in the Southern Altiplano (Uturuncu volcano, 22°S) between 65 and 14 ka constrained by cosmogenic ^{3}He dating. Quat. Res. 82, 209–221. doi:10.1016/j.yqres.2014.02.002

Blard, P.-H., Balco, G., Burnard, P.G., Farley, K.A., Fenton, C.R., Friedrich, R., Jull, A.J.T., Niedermann, S., Pik, R., Schaefer, J.M., Scott, E.M., Shuster, D.L., Stuart, F.M., Stute, M., Tibari, B., Winckler, G., Zimmermann, L., 2015. An inter-laboratory comparison of cosmogenic ^{3}He and radiogenic ^{4}He in the CRONUS-P pyroxene standard. Quat. Geochronol. 26, 11–19. doi:10.1016/j.quageo.2014.08.004

Bookhagen, B., Haselton, K., Trauth, M.H., 2001. Hydrological modelling of a Pleistocene landslide-dammed lake in the Santa Maria Basin, NW Argentina. Palaeogeogr. Palaeoclimatol. Palaeoecol. 169, 113–127. doi:10.1016/S0031-0182(01)00221-8

Bookhagen, B., Strecker, M.R., 2014. Evolution and erosional dynamics of intermontane basins on the Puna Plateau, NW Argentina. Am. Geophys. Union, Fall Meet. 2014, Abstr. #EP21B-3537.

Borchers, B., Marrero, S., Balco, G., Caffee, M., Goehring, B., Lifton, N., Nishiizumi, K., Phillips, F., Schaefer, J., Stone, J., 2016. Geological calibration of spallation production rates in the CRONUS-Earth project. Quat. Geochronol. 31, 188–198. doi:10.1016/j.quageo.2015.01.009

Bromley, G.R.M., Winckler, G., Schaefer, J.M., Kaplan, M.R., Licht, K.J., Hall, B.L., 2014. Pyroxene separation by HF leaching and its impact on helium surface-exposure dating. Quat. Geochronol. 23, 1–8. doi:10.1016/j.quageo.2014.04.003

Castino, F., Bookhagen, B., Strecker, M.R., 2016. Rainfall variability and trends of the past six decades (1950–2014) in the subtropical NW Argentine Andes. Clim. Dyn. 48, 1049-1067. doi:10.1007/s00382-016-3127-2

Delunel, R., Blard, P.-H., Martin, L.C.P., Nomade, S., Schlunegger, F., 2016. Long term low latitude and high elevation cosmogenic ^{3}He production rate inferred from a 107 ka-old lava flow in northern Chile; 22°S-3400 m a.s.l. Geochim. Cosmochim. Acta 184, 71–87. doi:10.1016/j.gca.2016.04.023

Fenton, C.R., Niedermann, S., Goethals, M.M., Schneider, B., Wijbrans, J., 2009. Evaluation of cosmogenic ^{3}He and ^{21}Ne production rates in olivine and pyroxene from two Pleistocene basalt flows, western Grand Canyon, AZ, USA. Quat. Geochronol. 4, 475–492. doi:10.1016/j.quageo.2009.08.002

Fritz, S.C., Baker, P.A., Lowenstein, T.K., Seltzer, G.O., Rigsby, C.A., Dwyer, G.S., Tapia, P.M., Arnold, K.K., Ku, T.L., Luo, S., 2004. Hydrologic variation during the last 170,000 years in the southern hemisphere tropics of South America. Quat. Res. 61, 95–104. doi:10.1016/j.yqres.2003.08.007

Fritz, S.C., Baker, P.A., Seltzer, G.O., Ballantyne, A., Tapia, P., Cheng, H., Edwards, R.L., 2007. Quaternary glaciation and hydrologic variation in the South American tropics as reconstructed from the Lake Titicaca drilling project. Quat. Res. 68, 410–420. doi:10.1016/j.yqres.2007.07.008

Garreaud, R., Vuille, M., Clement, A.C., 2003. The climate of the Altiplano: Observed current conditions and mechanisms of past changes. Palaeogeogr. Palaeoclimatol. Palaeoecol. 194, 5–22. doi:10.1016/S0031-0182(03)00269-4

Goethals, M.M., Hetzel, R., Niedermann, S., Wittmann, H., Fenton, C.R., Kubik, P.W., Christl, M., von Blanckenburg, F., 2009a. An improved experimental determination of cosmogenic ^{10}Be/^{21}Ne and ^{26}Al/^{21}Ne production ratios in quartz. Earth Planet. Sci. Lett. 284, 187–198. doi:10.1016/j.epsl.2009.04.027

Goethals, M.M., Niedermann, S., Hetzel, R., Fenton, C.R., 2009b. Determining the impact of faulting on the rate of erosion in a low-relief landscape: A case study using in situ produced ^{21}Ne on active normal faults in the Bishop Tuff, California. Geomorphology 103, 401–413. doi:10.1016/j.geomorph.2008.07.008

Gosse, J.C., Phillips, F.M., 2001. Terrestrial in situ cosmogenic nuclides: theory and application. Quat. Sci. Rev. 20, 1475–1560. doi:10.1016/S0277-3791(00)00171-2

Haselton, K., Hilley, G., Strecker, M.R., 2002. Average Pleistocene Climatic Patterns in the Southern Central Andes: Controls on Mountain Glaciation and Paleoclimate Implications. J. Geol. 110, 211–226. doi:10.1086/338414

Jomelli, V., Favier, V., Vuille, M., Braucher, R., Martin, L., Blard, P.-H., Colose, C., Brunstein, D., He, F., Khodri, M., Bourlès, D.L., Leanni, L., Rinterknecht, V., Grancher, D., Francou, B., Ceballos, J.L., Fonseca, H., Liu, Z., Otto-Bliesner, B.L., 2014. A major advance of tropical Andean glaciers during the Antarctic cold reversal. Nature 513, 224–228. doi:10.1038/nature13546

Kelly, M.A., Lowell, T. V., Applegate, P.J., Phillips, F.M., Schaefer, J.M., Smith, C.A., Kim, H., Leonard, K.C., Hudson, A.M., 2015. A locally calibrated, late glacial ^{10}Be production rate from a low-latitude, high-altitude site in the Peruvian Andes. Quat. Geochronol. 26, 70–85. doi:10.1016/j.quageo.2013.10.007

Lifton, N., Sato, T., Dunai, T.J., 2014. Scaling in situ cosmogenic nuclide production rates using analytical approximations to atmospheric cosmic-ray fluxes. Earth Planet. Sci. Lett. 386, 149–160. doi:10.1016/j.epsl.2013.10.052

Marrero, S.M., Phillips, F.M., Borchers, B., Lifton, N., Aumer, R., Balco, G., 2016. Cosmogenic nuclide systematics and the CRONUScalc program. Quat. Geochronol. 31, 160–187. doi:10.1016/j.quageo.2015.09.005

Martin, L.C.P., Blard, P.-H., Lavé, J., Braucher, R., Lupker, M., Condom, T., Charreau, J., Mariotti, V., Davy, E., 2015. In situ cosmogenic ^{10}Be production rate in the High Tropical Andes. Quat. Geochronol. 30, 54–68. doi:10.1016/j.quageo.2015.06.012

Martin, L.C.P., Blard, P.-H., Balco, G., Lavé, J., Delunel, R., Lifton, N., Laurent, V., 2016. The CREp program and the ICE-D production rate calibration database: A fully parameterizable and updated online tool to compute cosmic-ray exposure ages. Quat. Geochronol. 38, 25-49. doi:10.1016/j.quageo.2016.11.006

Masarik, J., 2002. Numerical simulation of in-situ production of cosmogenic nuclides. in: Goldschmidt Conference Abstracts. Geochim. Cosmochim. Acta 66, A491.

Matteini, M., Mazzuoli, R., Omarini, R., Cas, R., Maas, R., 2002. Geodynamical evolution of Central Andes at 24°S as inferred by magma composition along the Calama-Olacapato-El Toro transversal volcanic belt. J. Volcanol. Geotherm. Res. 118, 205–228. doi:10.1016/S0377-0273(02)00257-3

McGlue, M.M., Cohen, A.S., Ellis, G.S., Kowler, A.L., 2013. Late Quaternary stratigraphy, sedimentology and geochemistry of an underfilled lake basin in the Puna Plateau (northwest Argentina). Basin Res. 25, 638–658. doi:10.1111/bre.12025

Merchel, S., Herpers, U., 1999. An Update on Radiochemical Separation Techniques for the Determination of Long-Lived Radionuclides via Accelerator Mass Spectrometry. Radiochim. Acta 84, 215–220. doi:10.1524/ract.1999.84.4.215

Merchel, S., Bremser, W., Alfimov, V., Arnold, M., Aumaître, G., Benedetti, L., Bourlès, D.L., Caffee, M., Fifield, L.K., Finkel, R.C., Freeman, S.P.H.T., Martschini, M., Matsushi, Y., Rood, D.H., Sasa, K., Steier, P., Takahashi, T., Tamari, M., Tims, S.G., Tosaki, Y., Wilcken, K.M., Xu, S., 2011. Ultra-trace analysis of ^{36}Cl by accelerator mass spectrometry: An interlaboratory study. Anal. Bioanal. Chem. 400, 3125–3132. doi:10.1007/s00216-011-4979-2

Merchel, S., Bremser, W., Bourlès, D.L., Czeslik, U., Erzinger, J., Kummer, N.A., Leanni, L., Merkel, B., Recknagel, S., Schaefer, U., 2013a. Accuracy of ^{9}Be-data and its influence on ^{10}Be cosmogenic nuclide data. J. Radioanal. Nucl. Chem. 298, 1871–1878. doi:10.1007/s10967-013-2746-x

Merchel, S., Braucher, R., Alfimov, V., Bichler, M., Bourlès, D.L., Reitner, J.M., 2013b. The potential of historic rock avalanches and man-made structures as chlorine-36 production rate calibration sites. Quat. Geochronol. 18, 54–62. doi:10.1016/j.quageo.2013.07.004

Niedermann, S., 2002. Cosmic-Ray-Produced Noble Gases in Terrestrial Rocks: Dating Tools for Surface Processes. Rev. Mineral. Geochem. 47, 731–784. doi:10.2138/rmg.2002.47.16

Niedermann, S., Bach, W., Erzinger, J., 1997. Noble gas evidence for a lower mantle component in MORBs from the southern East Pacific Rise: Decoupling of helium and neon isotope systematics. Geochim. Cosmochim. Acta 61, 2697–2715. doi:10.1016/S0016-7037(97)00102-6

Nishiizumi, K., Imamura, M., Caffee, M.W., Southon, J.R., Finkel, R.C., McAninch, J., 2007. Absolute calibration of ^{10}Be AMS standards. Nucl. Instr. Meth. Phys. Res. Sect. B 258, 403–413. doi:10.1016/j.nimb.2007.01.297

Phillips, F.M., Kelly, M.A., Hudson, A.M., Stone, J.O.H., Schaefer, J., Marrero, S.M., Fifield, L.K., Finkel, R., Lowell, T., 2016. CRONUS-Earth calibration samples from the Huancané II moraines, Quelccaya Ice Cap, Peru. Quat. Geochronol. 31, 220–236. doi:10.1016/j.quageo.2015.10.005

Placzek, C., Quade, J., Patchett, P.J., 2006. Geochronology and stratigraphy of late Pleistocene lake cycles on the southern Bolivian Altiplano: Implications for causes of tropical climate change. Bull. Geol. Soc. Am. 118, 515–532. doi:10.1130/B25770.1

Poreda, R.J., Cerling, T.E., 1992. Cosmogenic neon in recent lavas from the western United States. Geophys. Res. Lett. 19, 1863–1866. doi:10.1029/92GL01998

Protin, M., Blard, P.-H., Marrocchi, Y., Mathon, F., 2016. Irreversible adsorption of atmospheric helium on olivine: A lobster pot analogy. Geochim. Cosmochim. Acta 179, 76–88. doi:10.1016/j.gca.2016.01.032

Rugel, G., Pavetich, S., Akhmadaliev, S., Enamorado Baez, S.M., Scharf, A., Ziegenrücker, R., Merchel, S., 2016. The first four years of the AMS-facility DREAMS: Status and developments for more accurate radionuclide data. Nucl. Instr. Meth. Phys. Res. Sect. B 370, 94–100. doi:10.1016/j.nimb.2016.01.012

Trauth, M.H., Bookhagen, B., Marwan, N., Strecker, M.R., 2003. Multiple landslide clusters record Quaternary climate changes in the northwestern Argentine Andes. Palaeogeogr. Palaeoclimatol. Palaeoecol. 194, 109–121. doi:10.1016/S0031-0182(03)00273-6

Vermeesch, P., Balco, G., Blard, P.-H., Dunai, T.J., Kober, F., Niedermann, S., Shuster, D.L., Strasky, S., Stuart, F.M., Wieler, R., Zimmermann, L., 2015. Interlaboratory comparison of cosmogenic ^{21}Ne in quartz. Quat. Geochronol. 26, 20–28. doi:10.1016/j.quageo.2012.11.009

Zech, J., Zech, R., Kubik, P.W., Veit, H., 2009. Glacier and climate reconstruction at Tres Lagunas, NW Argentina, based on ^{10}Be surface exposure dating and lake sediment analyses. Palaeogeogr. Palaeoclimatol. Palaeoecol. 284, 180–190. doi:10.1016/j.palaeo.2009.09.023

Supplementary Materials

Glacial chronology and production rate cross-calibration of five cosmogenic nuclide and mineral systems from the southern Central Andean Plateau

Authors and Affiliations

Lisa V. Luna[1], Bodo Bookhagen[1], Samuel Niedermann[2], Georg Rugel[3], Andreas Scharf[3], Silke Merchel[3]

[1]University of Potsdam, Institute of Earth and Environmental Science, Karl-Liebknecht-Str. 24-25, 14476 Potsdam-Golm, Germany

[2]GFZ German Research Center for Geosciences, Telegrafenberg, 14473 Potsdam, Germany

[3]Helmholtz-Zentrum Dresden-Rossendorf, Bautzner Landstraße 400, 01328 Dresden, Germany

Corresponding author: Bodo Bookhagen, bodo.bookhagen@uni-potsdam.de

- Figures
- Text
- References
- Appendix Tables
- Boulder Library

Supplementary Figures

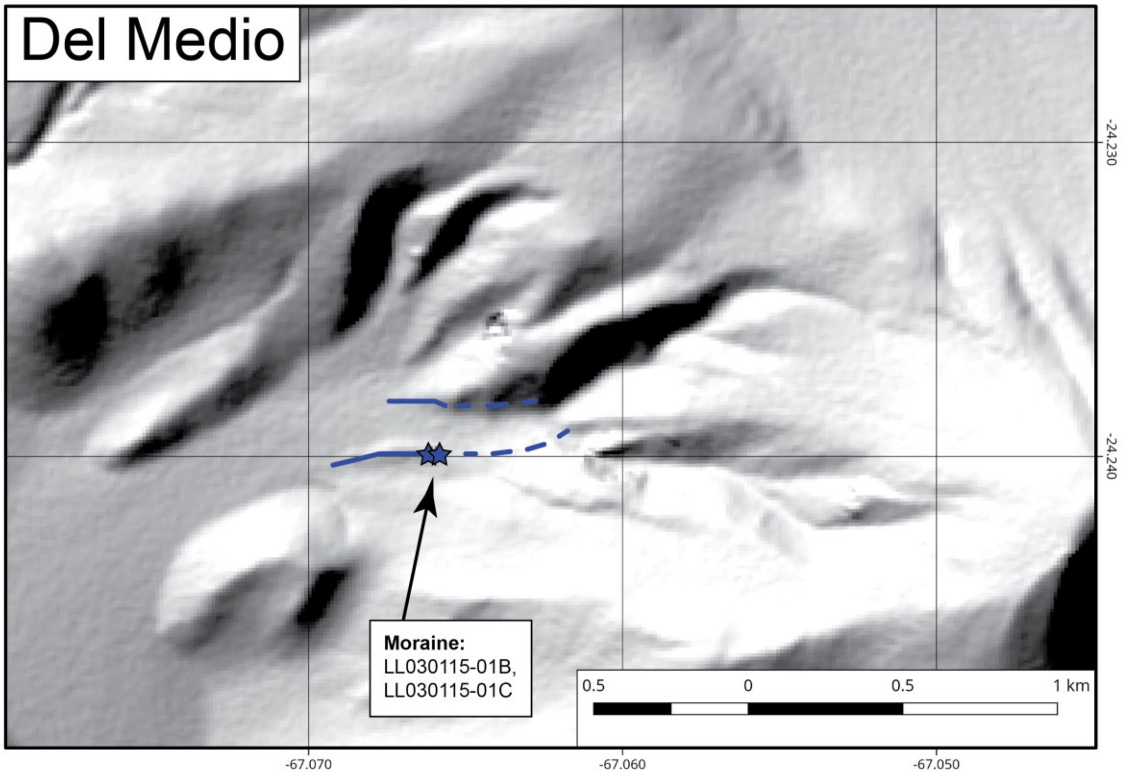

Figure A1 – Geomorphic map of the Del Medio valley. In figures A1 through A4, the relative moraine ages are indicated by colors, ranging from the blue (oldest) to light red (younger) to dark red (youngest). Dashed lines indicate estimated moraine deposits based on landform, structure and field investigations. Solid lines indicate moraine deposits that have been clearly identified as such during field work. Background images are hillshades of TanDEM-X.

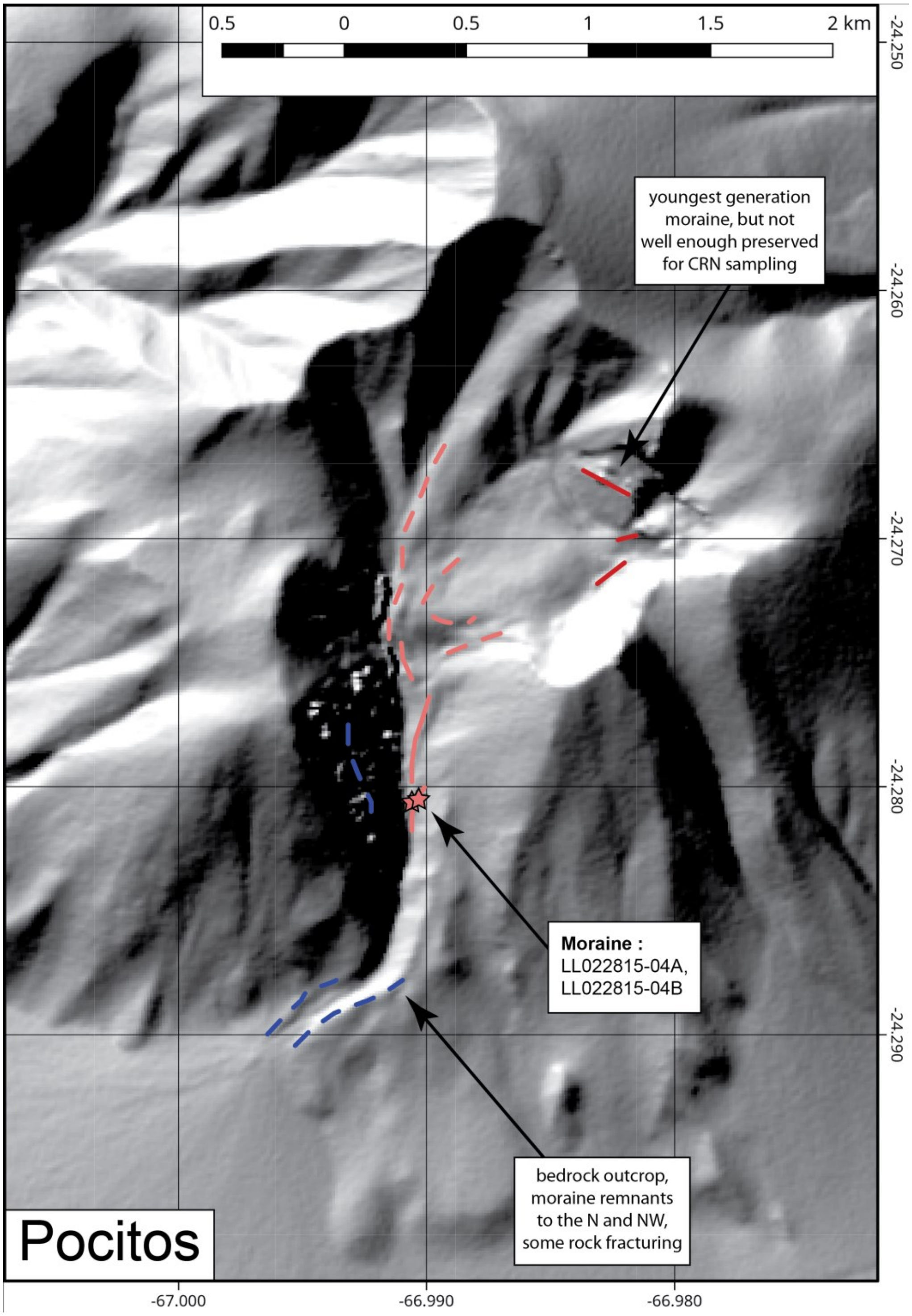

Figure A2 – Geomorphic map of the Pocitos valley. In figures A1 through A4, the relative moraine ages are indicated by colors, ranging from the blue (oldest) to light red (younger) to dark red (youngest). Dashed lines indicate estimated moraine deposits based on landform, structure and field investigations. Solid lines indicate moraine deposits that have been clearly identified as such during field work. Background images are hillshades of TanDEM-X.

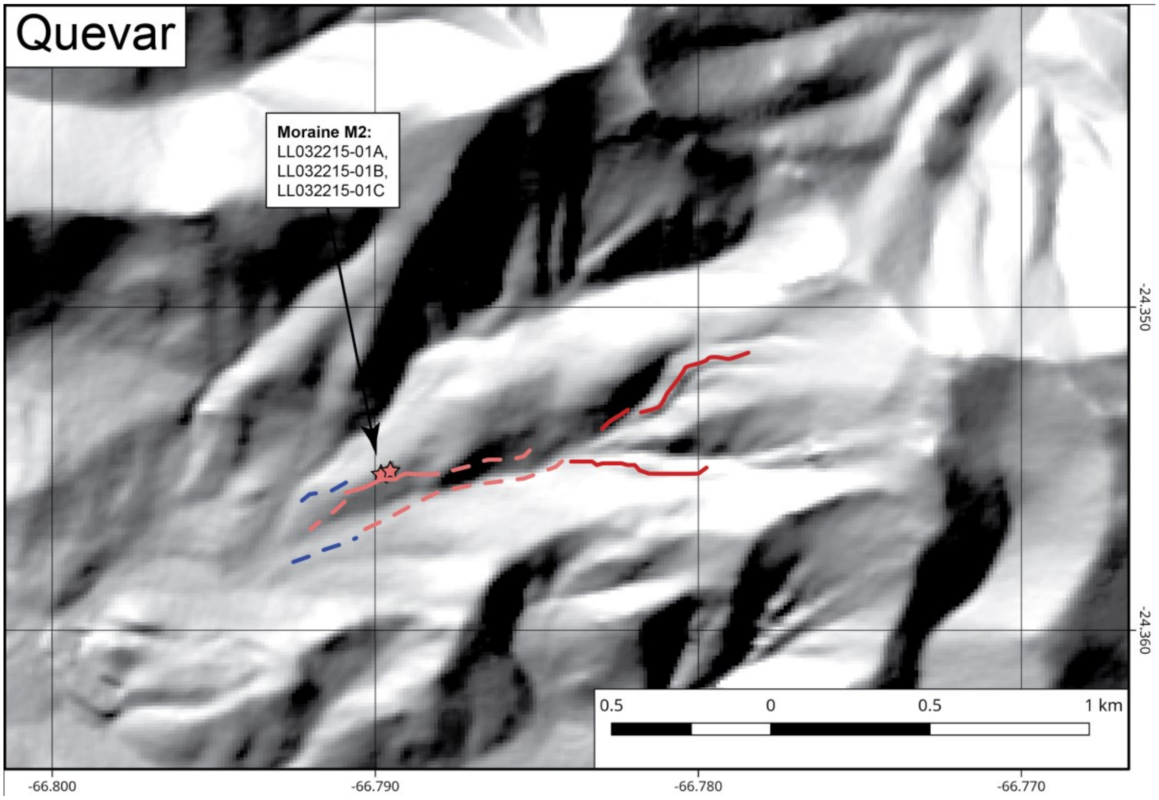

Figure A3 – Geomorphic map of the Quevar valley. In figures A1 through A4, the relative moraine ages are indicated by colors, ranging from the blue (oldest) to light red (younger) to dark red (youngest). Dashed lines indicate estimated moraine deposits based on landform, structure and field investigations. Solid lines indicate moraine deposits that have been clearly identified as such during field work. Background images are hillshades of TanDEM-X.

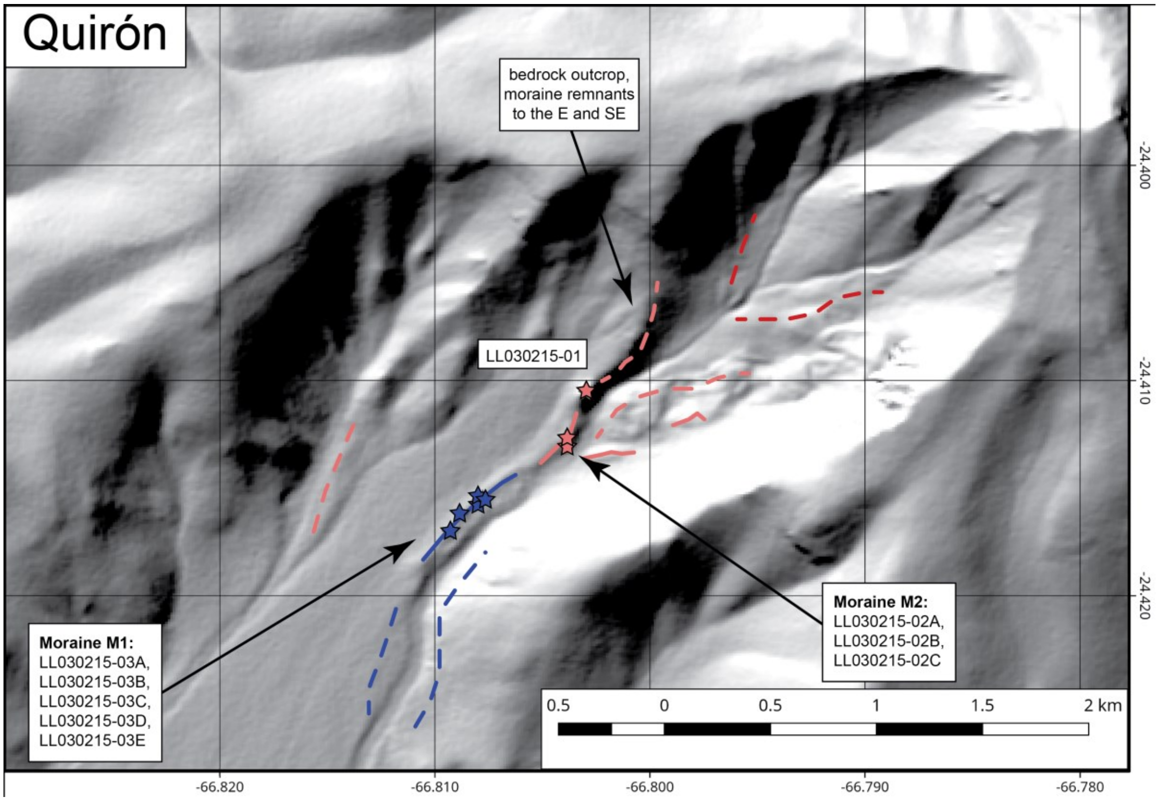

Figure A4 – Geomorphic map of the Quirón valley. In figures A1 through A4, the relative moraine ages are indicated by colors, ranging from the blue (oldest) to light red (younger) to dark red (youngest). Dashed lines indicate estimated moraine deposits based on landform, structure and field investigations. Solid lines indicate moraine deposits that have been clearly identified as such during field work. Background images are hillshades of TanDEM-X.

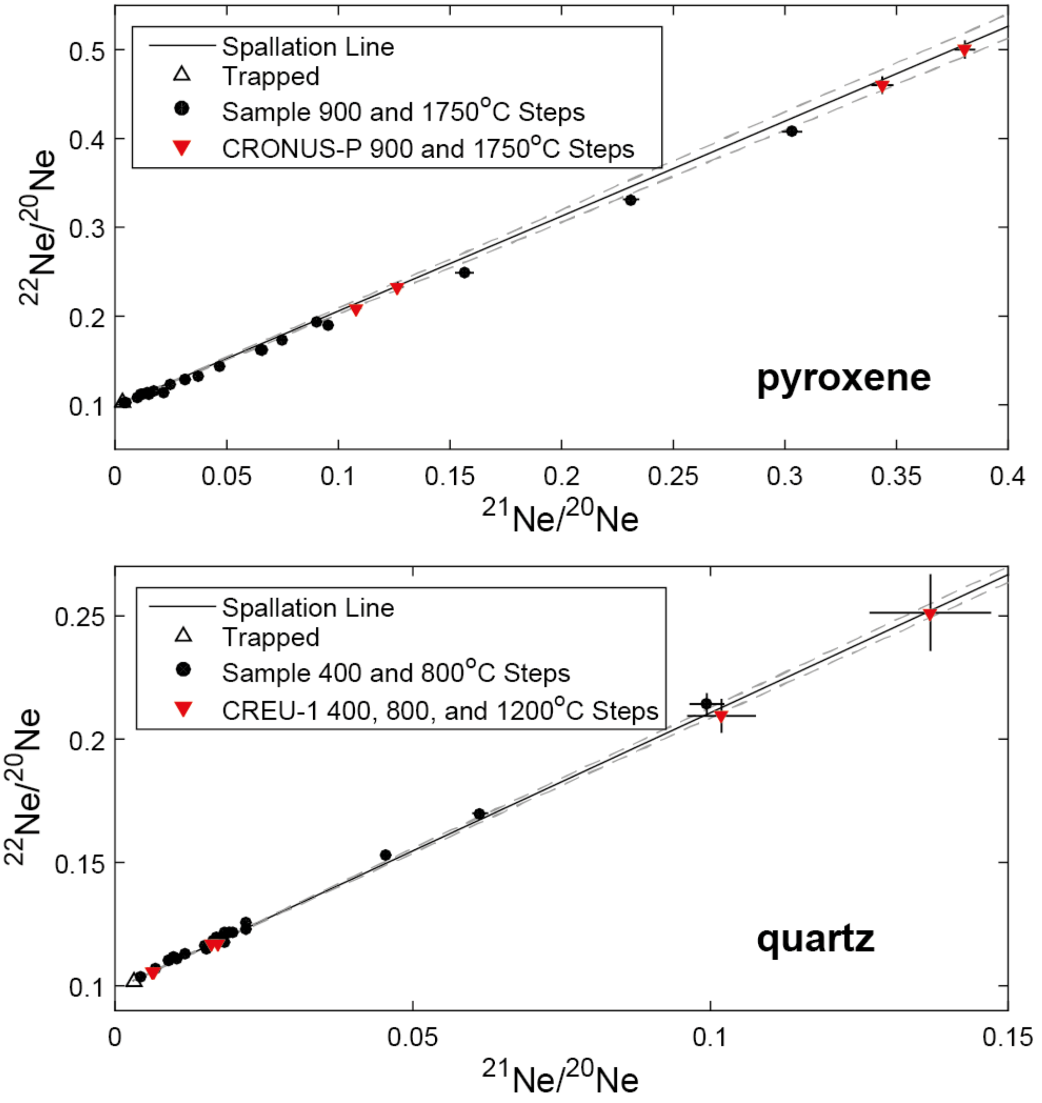

Figure A5 - Neon three-isotope plots for pyroxene and quartz. Neon three-isotope plots show the compositions of various Ne components (e.g., mantle Ne, crustal Ne, and cosmogenic Ne). The spallation line represents a mixture of cosmogenic and atmospheric Ne, and its slope has been experimentally determined for quartz (1.120 ± 0.021, Niedermann et al., 1993) and pyroxene (1.069 ± 0.035, Schäfer et al., 1999). The stepwise heating results for both the pyroxene and quartz samples plot very near to the spallation line, indicating no contribution from nucleogenic Ne. Although some quartz samples plot slightly above the spallation line, CREU-1 analyses plot on or slightly below the line, indicating that the higher $^{22}Ne/^{20}Ne$ ratios are not due to an experimental artifact. CRONUS-P (Blard et al., 2015) and CREU-1 (Vermeesch et al., 2015) are quality assurance samples from the CRONUS-Earth and CRONUS-EU projects.

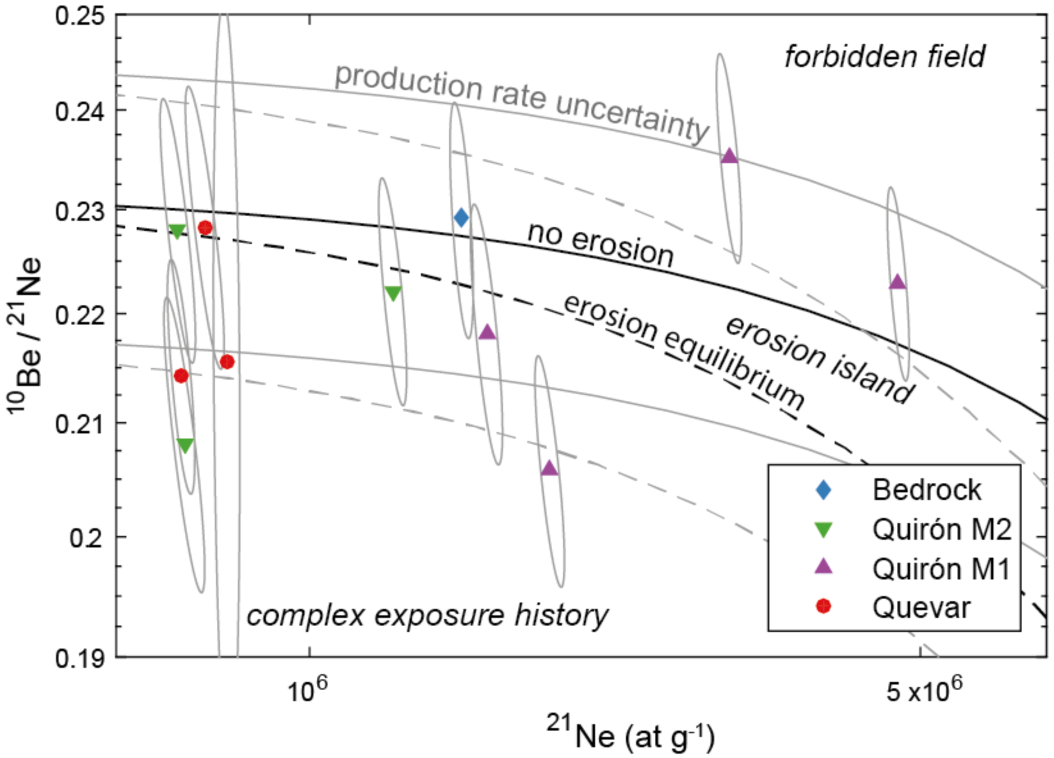

Figure A6 - $^{21}Ne_{qtz}/^{10}Be$ Two-nuclide plot ('banana plot'). Two nuclide plots (e.g., Lal, 1991) predict the ratio of one nuclide to another given a certain exposure scenario, and can show if a sample has been pre-exposed and then buried. Samples with a simple exposure scenario plot within the "erosion island", i.e. the area bounded by the "no erosion" and "erosion equilibrium" lines. Black lines indicate the position of the erosion island based on the production rates used in this study. Gray lines indicate the minimum and maximum positions of the erosion island considering the production rate uncertainties. Concentrations were normalized by their site-specific topographic and time-dependent geographic scaling factors in order to compare all samples on the same plot. All samples plot within uncertainty of the erosion island, considering uncertainty on the production rates, indicating that they have had a simple exposure history. However, the analytical uncertainty overlaps a large range of erosion rate – exposure age combinations, making it impossible to simultaneously calculate these values. Error ellipses were calculated following Balco et al. (2008).

Supplementary Text

S1 AMS Standardization for ^{10}Be, ^{26}Al, and ^{36}Cl Measurements

All AMS measurements were performed at the DREAMS facility at HZDR. All ratios were either normalized to standards or to in-house standards that have been cross-calibrated against primary standards.

^{10}Be/^{9}Be ratios were normalized to in-house standard SMD-Be-12 (Akhmadaliev et al., 2013), which has been cross-calibrated to the NIST SRM 4325 standard (^{10}Be/^{9}Be ratio of $2.79 \pm 0.03 \times 10^{-11}$) (Nishiizumi et al., 2007).

^{26}Al/^{27}Al ratios were normalized to SMD-Al-11 (Rugel et al., 2016). SMD-Al-11 ($9.66 \pm 0.14 \times 10^{-12}$ ^{26}Al/^{27}Al) is a secondary in-house standard that was produced by dilution with stable ^{27}Al from a solution containing ~1.4 Bq of ^{26}Al. It was calibrated against three primary standards at different ratio levels (MB04-A, MB04-B, and MB04-D), following the approach of Arnold et al., 2010. The values for the primary standards were determined through a round-robin exercise involving eight AMS laboratories (Merchel and Bremser, 2004).

^{36}Cl/^{35}Cl ratios were normalized to the primary-type SM-Cl-12 standard. Similar to the Al standards, the ratio of the primary standard was determined through a round-robin exercise with eight participating AMS laboratories (Merchel et al., 2011).

S2 Estimating Cosmogenic ^{3}He Concentrations

The total measured ^{3}He in a pyroxene sample stems from three sources: trapped ^{3}He, which is magmatic, crustal or atmospheric gas trapped in fluid inclusions or in the lattice, nucleogenic and cosmogenic thermal neutron produced ^{3}He, which is produced by the interaction of thermal neutrons with ^{6}Li, and spallation produced cosmogenic ^{3}He (e.g., Niedermann, 2002; Dunai et al., 2007). The total measured ^{4}He in a sample is a combination of ^{4}He that was trapped upon formation and radiogenic ^{4}He produced through the decay of U and Th. In order to estimate the amount of spallation-produced cosmogenic ^{3}He ($^{3}He_{sp}$) in a sample, we must first correct for the other sources.

The concentration of $^{3}He_{sp}$ in a sample can be expressed by the following equation (Blard and Farley, 2008):

$$^{3}He_{sp} = \,^{3}He_{m} - \int_{0}^{T_e} P_{ctn} \times dt + \int_{0}^{T_c} P_{rtn} \,\times dt) - (\,^{4}He_{m} - \int_{0}^{T_c} P_{4} \times dt) \times \left(\frac{^{3}He}{^{4}He}\right)_{tr}$$

Equation S1

where $^{3}He_{m}$ is the total measured ^{3}He released by step heating, T_e is the exposure age of the rock, P_{ctn} is the ^{3}He production rate from cosmogenic thermal neutrons, T_c is the He closure age of the rock (formation age), P_{rtn} is the nucleogenic ^{3}He production rate from radiogenic thermal neutrons, $^{4}He_{m}$ is the total measured ^{4}He released during step heating, P_4 is the production rate of radiogenic ^{4}He, and $(^{3}He/^{4}He)_{tr}$ is the isotope ratio of the trapped He component.

S1.1 Trapped $^{3}He/^{4}He$ ratio

Since the crushing extractions yielded unrealistic values for $(^{3}He/^{4}He)_{tr}$ between 0.33×10^{-6} and 80×10^{-6}, we prefer to use a literature value for the ratio of 7.77×10^{-6} or 5.55 Ra (reported normalized to the air $^{3}He/^{4}He$ ratio $Ra=1.39\times10^{-6}$), which is a mean value from clinopyroxene phenocrysts from three nearby sites on the Puna (Hilton et al., 1993; Pilz, 2008). As discussed in the next section, this value has a negligible impact on the age determinations.

S1.2 Radiogenic ^{4}He and Trapped ^{3}He

Radiogenic ^{4}He ($^{4}He^{*}$) produced by decay of U and Th was calculated following Blard and Farley (2008). First, the production rate of ^{4}He (at g^{-1} yr^{-1}) in both the rock matrix (M_4) and the mineral of interest (I_4) resulting from the decay of U and Th was calculated according to the following equation:

$$I_4 or\ M_4 = 8 \times \left[^{238}U\right] \times \lambda_{238} + 7 \times \left[^{235}U\right] \times \lambda_{235} + 6 \times \left[^{232}Th\right] \times \lambda_{232}$$

Equation S2

where $[^{i}X]$ is the concentration in either the mineral of interest or host rock (at g^{-1}) and λ_i is the decay constant (yr^{-1}). The range of α-particles in pyroxene is approximately 20 μm, meaning that some ^{4}He produced in the rock matrix may be implanted into the pyroxene crystals, and some ^{4}He produced in the mineral may be ejected into the matrix. Since the U and Th concentrations in the rock matrix are in some cases up to 650 times higher than those in the pyroxene crystals, implanted ^{4}He* is the dominant source of ^{4}He* in these samples. To calculate the total production rate of ^{4}He* in the crystal, the equations for ejection (Farley et al., 1996) and implantation (Dunai and Wijbrans, 2000) are combined (Blard and Farley, 2008):

$$P_4 = I_4 \times \left[1 - 1.5 \times \left(\frac{S}{D}\right) + 0.5 \times \left(\frac{S}{D}\right)^3\right] + M_4 \times \left[1.5 \times \left(\frac{S}{D}\right) - 0.5 \times \left(\frac{S}{D}\right)^3\right]$$

Equation S3

where P_4 is the total production rate in the pyroxene crystal (at g^{-1} yr^{-1}), S is the α-particle stopping distance (μm), and D is the equivalent diameter of a sphere (μm). Since this equation is for implantation and ejection from a sphere, and pyroxene crystals are not spherical, the equivalent diameter of a sphere must be found for our samples. The crystals ranged from 125-500 μm in width, so we take 300 μm as a representative width for the samples, corresponding to a sphere diameter (D) of 300 μm (Farley and Stockli, 2002). A smaller width corresponds to a higher production rate for ^{4}He*, and a larger width to a lower rate. 300 μm thus produces a conservatively low estimate for the production rate, as qualitative observation of the crystals during hand-picking suggests that most crystals are narrower than 300 μm.

Literature values for the formation ages of the rocks from these volcanoes range from 5-8 Ma (Matteini et al., 2002). We assume a closure age for He of 8 Ma, which leads to a higher predicted concentration of radiogenic ^{4}He*.

Predicted ^{4}He* concentrations are higher than the total measured ^{4}He concentrations for all samples except LL022815-04A (Table A7). The predicted concentrations range from 160 – 510% of the measured concentrations, except for LL022815-04A, where the predicted concentration is 29% of measured. If we assume a closure age of 5 Ma, the predicted concentrations range from 100% - 320% of the measured concentrations, except for LL022815-04A. The discrepancy between the predicted and measured concentrations is most likely explained by loss of material from the surface of the crystals through leaching. Because the major source of radiogenic ^{4}He* in these samples is implanted ^{4}He, which is concentrated in the outer rim (in situ production accounts for only several percent of total production in most samples), removing even 10 μm of material from the surface of the crystal results in a ~40-50% decrease in total predicted ^{4}He*. Our measured ^{4}He concentrations are consistent with the hypothesis that some material was removed through leaching, but not enough to completely remove the implanted ^{4}He* component. Furthermore, as each sample was leached for differing amounts of time depending on the initial pyroxene purity after magnetic and heavy liquid separation, it is not surprising that the ratio of the predicted concentration to the measured concentration varies between samples (Bromley et al., 2014). Differing grain size distributions between samples may also play a role. Bromley et al. (2014) observed a two-fold decrease in ^{4}He concentrations between non-leached and leached samples, which they suggest improves the estimation of the trapped ^{3}He component by reducing the radiogenic ^{4}He component. Although it is indeed critical to correctly account for radiogenic ^{4}He, our results demonstrate that leaching must be sufficient to remove the entire implanted component, otherwise it is very difficult to estimate how much of the remaining ^{4}He is radiogenic. In this case, between one and three leaching cycles over 4-6 hours in 1% HF/1% HNO_3 in an ultrasonic bath was not sufficient to completely remove the implanted radiogenic ^{4}He component.

Although the exact contribution of ^{4}He* is difficult to predict in these samples, the consistently higher predicted values with respect to the measured values suggest that the vast majority of ^{4}He is radiogenic. The $^4He_{tr}$ component is likely to be very small when compared with the total measured ^{4}He. This is consistent with the small crystal size of these samples (<500 μm), which some studies have suggested should have very low concentrations of trapped He (Williams et al., 2005). Furthermore, the concentrations of ^{4}He released by heating were often two orders of magnitude higher than those released by crushing, which is typical of samples dominated by radiogenic ^{4}He. It then follows that the concentration of trapped ^{3}He is also small with respect to the total measured ^{3}He. Even if the $^4He_{tr}$ component were 2% of the total measured ^{4}He, the resulting concentration of $^3He_{tr}$ (assuming a $(^3He/^4He)_{tr}$ ratio of 7.77×10^{-6}) would be < 2% of the measured ^{3}He for all samples except LL030215-02B, where it would be 5%.

As these values are similar to the analytical uncertainty for ^{3}He concentrations, and far less than uncertainties of the resulting ages, we make no correction for trapped ^{3}He and assume that all measured ^{3}He is either cosmogenic or nucleogenic in origin. Doing so should have a negligible effect on the resulting production ratio or age calculations.

S2.3 Thermal Neutron Produced ^{3}He

^{3}He produced by thermal neutron absorption by ^{6}Li was corrected for following Andrews et al. (1986). Li concentrations in the pyroxene samples range from 22-71 μg g^{-1}. The thermal neutrons that interact with ^{6}Li to produce ^{3}H, which then decays to ^{3}He, can be produced in two ways: from secondary cosmogenic neutrons ('cosmogenic thermal neutrons') and from (α,n) reactions within the rock ('radiogenic thermal neutrons') (Dunai et al., 2007). The production rate from each of these sources was determined using the following equation:

$$P_{3He,rtn\ or\ ctn} = N_{Li} \times \sigma \times \Phi_{\text{rtn or ctn}}$$

Equation S4

where $P_{3He,rtn}$ or $P_{3He,ctn}$ is the production rate of ^{3}He from radiogenic thermal neutrons or cosmogenic thermal neutrons (at g^{-1} yr^{-1}), respectively, N_{Li} is the concentration of Li in the rock (at g^{-1}), σ is the cross section of the ^{6}Li(n,α)^{3}H reaction (cm^2), and $\Phi_{\text{rtn or ctn}}$ is the neutron flux (cm^{-2} yr^{-1}) for either radiogenic or cosmogenic thermal neutrons. The cosmogenic and radiogenic thermal neutron fluxes were calculated using algorithms from CRONUScalc, originally intended to do the same calculations for production of ^{36}Cl from thermal neutron absorption on ^{35}Cl (Marrero et al., 2016). No geometric corrections were made for implantation or ejection of ^{3}H. Production was calculated along a depth profile, and erosion was simulated by moving the sample up through the profile. For the contribution from cosmogenic thermal neutrons, an erosion rate of 1 mm kyr^{-1} and the ^{10}Be exposure age of the sample were used when available, otherwise the ^{21}Ne$_{px}$ age was used. For the contribution from radiogenic thermal neutrons, a rock formation age of 8 Ma was used.

Depending on the concentration of Li in the pyroxenes and the exposure age of the sample, the contribution of total thermal-neutron produced ^{3}He ranged from 6-13% of the measured ^{3}He. Radiogenic thermal-neutron produced ^{3}He accounted for 2-45% of the total thermal neutron produced ^{3}He.

S3 Production Ratio Calculations

For radioactive nuclides, decay and erosion must be corrected for in order to determine the ratio of production rates. For stable nuclides, the ratio is not affected by erosion and no correction is needed. To calculate the production-rate ratio for two nuclides, at least one of which is radioactive, the following equation was used (Gosse and Phillips, 2001):

$$\frac{P_1}{P_2} = \frac{N_1\left(1 - e^{-\left(\lambda_2 + \frac{\varepsilon\rho}{\Lambda}\right)t}\right)\left(\lambda_1 + \frac{\varepsilon\rho}{\Lambda}\right)}{N_2\left(1 - e^{-\left(\lambda_1 + \frac{\varepsilon\rho}{\Lambda}\right)t}\right)\left(\lambda_2 + \frac{\varepsilon\rho}{\Lambda}\right)}$$

Equation S5

where P_1/P_2 is the production ratio of nuclide 1 and nuclide 2, N_i is the concentration of nuclide *i* in the rock (at g^{-1}), λ_i is the decay constant (yr^{-1}), ε is the erosion rate (cm yr^{-1}), ρ is the density of the rock (g cm^{-3}), Λ is the attenuation length (g cm^{-2}), and t is the exposure age (yr). We used an erosion rate of 1 mm kyr^{-1} and the ^{10}Be exposure age for each sample. In the case that both nuclides are stable, the equation simplifies to:

$$\frac{P_1}{P_2} = \frac{N_1}{N_2}$$

Equation S6

Supplementary References

Akhmadaliev, S., Heller, R., Hanf, D., Rugel, G., Merchel, S., 2013. The new 6 MV AMS-facility DREAMS at Dresden. Nucl. Instr. Meth. Phys. Res. Sect. B 294, 5–10. doi:10.1016/j.nimb.2012.01.053

Andrews, J.N., Fontes, J.C., Michelot, J.L., Elmore, D., 1986. In-situ neutron flux, ^{36}Cl production and groundwater evolution in crystalline rocks at Stripa, Sweden. Earth Planet. Sci. Lett. 77, 49–58. doi:10.1016/0012-821X(86)90131-7

Arnold, M., Merchel, S., Bourles, D.L., Braucher, R., Benedetti, L., Finkel, R.C., Aumaitre, G., Gottdang, A., Klein, M., 2010. The French accelerator mass spectrometry facility ASTER: Improved performance and developments. Nucl. Instr. Meth. Phys. Res. Sect. B 268, 1954–1959. doi:10.1016/j.nimb.2010.02.107

Balco, G., Stone, J.O.H., Lifton, N., Dunai, T.J., 2008. A complete and easily accessible means of calculating surface exposure ages or erosion rates from ^{10}Be and ^{26}Al measurements. Quat. Geochronol. 3, 174–195.

Blard, P.H., Farley, K.A., 2008. The influence of radiogenic ^{4}He on cosmogenic ^{3}He determinations in volcanic olivine and pyroxene. Earth Planet. Sci. Lett. 276, 20–29. doi:10.1016/j.epsl.2008.09.003

Blard, P.H., Balco, G., Burnard, P.G., Farley, K.A., Fenton, C.R., Friedrich, R., Jull, A.J.T., Niedermann, S., Pik, R., Schaefer, J.M., Scott, E.M., Shuster, D.L., Stuart, F.M., Stute, M., Tibari, B., Winckler, G., Zimmermann, L., 2015. An inter-laboratory comparison of cosmogenic ^{3}He and radiogenic ^{4}He in the CRONUS-P pyroxene standard. Quat. Geochronol. 26, 11–19. doi:10.1016/j.quageo.2014.08.004

Bromley, G.R.M., Winckler, G., Schaefer, J.M., Kaplan, M.R., Licht, K.J., Hall, B.L., 2014. Pyroxene separation by HF leaching and its impact on helium surface-exposure dating. Quat. Geochronol. 23, 1–8. doi:10.1016/j.quageo.2014.04.003

Dunai, T.J., Wijbrans, J.R., 2000. Long-term cosmogenic ^{3}He production rates (152 ka–1.35 Ma) from ^{40}Ar/^{39}Ar dated basalt flows at 29°N latitude. Earth Planet. Sci. Lett. 176, 147–156. doi:10.1016/S0012-821X(99)00308-8

Dunai, T.J., Stuart, F.M., Pik, R., Burnard, P., Gayer, E., 2007. Production of ^{3}He in crustal rocks by cosmogenic thermal neutrons. Earth Planet. Sci. Lett. 258, 228–236. doi:10.1016/j.epsl.2007.03.031

Farley, K.A., Wolf, R.A., Silver, L.T., 1996. The effects of long alpha-stopping distances on (U-Th)/He ages. Geochim. Cosmochim. Acta 60, 4223–4229. doi:10.1016/S0016-7037(96)00193-7

Farley, K.A., Stockli, D.F., 2002. (U-Th)/He Dating of Phosphates: Apatite, Monazite, and Xenotime. Rev. Mineral. Geochem. 48, 559–577. doi:10.2138/rmg.2002.48.15

Gosse, J.C., Phillips, F.M., 2001. Terrestrial in situ cosmogenic nuclides: theory and application. Quat. Sci. Rev. 20, 1475–1560. doi:10.1016/S0277-3791(00)00171-2

Hilton, D., Hammerschmidt, K., Teufel, S., Friedrichsen, H., 1993. Helium isotope characteristics of Andean geothermal fluids and lavas. Earth Planet. Sci. Lett. 120, 265–282.

Lal, D., 1991. Cosmic ray labeling of erosion surfaces: in situ nuclide production rates and erosion models. Earth Planet. Sci. Lett. 104, 424–439. doi:10.1016/0012-821X(91)90220-C

Pilz, P., 2008. Ein neues magmatisch-tektonisches Modell zur Asthenosphärendynamik im Bereich der zentralandinen Subduktionszone Südamerikas. Ph. D. thesis, Universität Potsdam.

Matteini, M., Mazzuoli, R., Omarini, R., Cas, R., Maas, R., 2002. Geodynamical evolution of Central Andes at 24°S as inferred by magma composition along the Calama-Olacapato-El Toro transversal volcanic belt. J. Volcanol. Geotherm. Res. 118, 205–228. doi:10.1016/S0377-0273(02)00257-3

Marrero, S.M., Phillips, F.M., Borchers, B., Lifton, N., Aumer, R., Balco, G., 2016. Cosmogenic nuclide systematics and the CRONUScalc program. Quat. Geochronol. 31, 160–187. doi:10.1016/j.quageo.2015.09.005

Merchel, S., Bremser, W., 2004. First international ^{26}Al interlaboratory comparison – Part I. Nucl. Instr. Meth. Phys. Res. Sect. B 223-224, 393–400. doi:10.1016/j.nimb.2004.04.076

Merchel, S., Bremser, W., Alfimov, V., Arnold, M., Aumaître, G., Benedetti, L., Bourlès, D.L., Caffee, M., Fifield, L.K., Finkel, R.C., Freeman, S.P.H.T., Martschini, M., Matsushi, Y., Rood, D.H., Sasa, K., Steier, P., Takahashi, T., Tamari, M., Tims, S.G., Tosaki, Y., Wilcken, K.M., Xu, S., 2011. Ultra-trace analysis of ^{36}Cl by accelerator mass spectrometry: An interlaboratory study. Anal. Bioanal. Chem. 400, 3125–3132. doi:10.1007/s00216-011-4979-2

Merchel, S., Bremser, W., Bourlès, D.L., Czeslik, U., Erzinger, J. , Kummer, N.-A., Leanni,L., Merkel, B., Recknagel, S., Schaefer, U. (2013): Accuracy of 9Be-data and its influence on 10Be cosmogenic nuclide data, J. Radioanal. Nucl. Chem. 298, 1871-1878

Niedermann, S., Graf, T., Marti, K., 1993. Mass spectrometric identification of cosmic-ray-produced neon in terrestrial rocks with multiple neon components. Earth Planet. Sci. Lett. 118, 65–73. doi:10.1016/0012-821X(93)90159-7

Niedermann, S., 2002. Cosmic-Ray-Produced Noble Gases in Terrestrial Rocks: Dating

Tools for Surface Processes. Rev. Mineral. Geochem. 47, 731–784. doi:10.2138/rmg.2002.47.16

Nishiizumi, K., Imamura, M., Caffee, M.W., Southon, J.R., Finkel, R.C., McAninch, J., 2007. Absolute calibration of ^{10}Be AMS standards. Nucl. Instr. Meth. Phys. Res. Sect. B 258, 403–413. doi:10.1016/j.nimb.2007.01.297

Rugel, G., Pavetich, S., Akhmadaliev, S., Enamorado Baez, S.M., Scharf, A., Ziegenrücker, R., Merchel, S., 2016. The first four years of the AMS-facility DREAMS: Status and developments for more accurate radionuclide data. Nucl. Instr. Meth. Phys. Res. Sect. B 370, 94–100. doi:10.1016/j.nimb.2016.01.012

Schäfer, J.M., Ivy-Ochs, S., Wieler, R., Leya, I., Baur, H., Denton, G.H., Schlüchter, C., 1999. Cosmogenic noble gas studies in the oldest landscape on earth: surface exposure ages of the Dry Valleys, Antarctica. Earth Planet. Sci. Lett. 167, 215–226. doi:10.1016/S0012-821X(99)00029-1

Vermeesch, P., Balco, G., Blard, P.H., Dunai, T.J., Kober, F., Niedermann, S., Shuster, D.L., Strasky, S., Stuart, F.M., Wieler, R., Zimmermann, L., 2015. Interlaboratory comparison of cosmogenic ^{21}Ne in quartz. Quat. Geochronol. 26, 20–28.

Williams, A.J., Stuart, F.M., Day, S.J., Phillips, W.M., 2005. Using pyroxene microphenocrysts to determine cosmogenic ^{3}He concentrations in old volcanic rocks: an example of landscape development in central Gran Canaria. Quat. Sci. Rev. 24, 211–222. doi:10.1016/j.quascirev.2004.07.004

Table A1: Be and Al data from quartz

Sample Name	Batch	DREAMS Be Name	DREAMS Al Name	Quartz Mass	^{9}Be Carrier Solution Added[1]	^{27}Al Carrier Solution Added[2]	ICP-Quantified Total Al	Measured ^{10}Be/^{9}Be ratio[3]	^{10}Be/^{9}Be ratio unc.	Measured ^{26}Al/^{27}Al ratio[4]	^{26}Al/^{27}Al ratio unc.	^{10}Be (blk. corr)	^{10}Be unc. (1σ)	^{26}Al (blk. corr)	^{26}Al unc. (1σ)
				g	g	g	µg		1σ		1σ	atoms/g	atoms/g	atoms/g	atoms/g
LL030215-01	B	B1477	A0527	3.66715	0.14076	0.75618	1371	8.98E-13	2.4E-14	3.670E-12	9.6E-14	5.15E+06	1.4E+05	3.05E+07	1.2E+06
LL030215-02A	A	B1465	A0515	8.06309	0.14048	0.75674	1909	1.534E-12	3.2E-14	4.038E-12	8.7E-14	4.055E+06	8.6E+04	2.158E+07	8.0E+05
LL030215-02B	A	B1466	A0516	7.08652	0.14035	0.75628	2021	6.50E-13	1.4E-14	1.740E-12	5.2E-14	1.936E+06	4.3E+04	1.111E+07	4.7E+05
LL030215-02C	A	B1467	A0517	8.04624	0.14037	0.75639	2025	8.17E-13	1.7E-14	2.254E-12	5.9E-14	2.135E+06	4.7E+04	1.264E+07	5.0E+05
LL030215-03A	B	B1472	A0522	2.60844	0.14091	0.75578	1056	5.73E-13	1.3E-14	2.956E-12	7.7E-14	4.63E+06	1.1E+05	2.66E+07	1.1E+06
LL030215-03B	B	B1473	A0523	7.72300	0.14090	0.75676	1676	1.959E-12	4.0E-14	6.47E-12	1.4E-13	5.37E+06	1.1E+05	3.14E+07	1.2E+06
LL030215-03C	B	B1474	A0524	1.68925	0.14086	0.75676	929	6.92E-13	1.5E-14	3.95E-12	1.0E-13	8.62E+06	1.9E+05	4.83E+07	1.9E+06
LL030215-03D	B	B1475	A0525	3.41778	0.14060	0.76685	1129	1.614E-12	3.2E-14	7.56E-12	1.6E-13	9.95E+06	2.0E+05	5.57E+07	2.1E+06
LL030215-03E	B	B1476	A0526	3.49946	0.14076	0.57584	974	2.475E-12	5.0E-14	1.428E-11	3.0E-13	1.491E+07	3.1E+05	8.86E+07	3.2E+06
LL032215-01A	A	B1468	A0518	7.35064	0.14058	0.75647	4408	1.03E-12	1.2E-13	1.01E-12	2.5E-13	2.96E+06	3.4E+05	1.35E+07	3.4E+06
LL032215-01B	A	B1469	A0519	6.32806	0.14096	1.00847	2287	8.57E-13	1.8E-14	2.178E-12	5.8E-14	2.872E+06	6.3E+04	1.763E+07	7.1E+05
LL032215-01C	A	B1470	A0520	2.85154	0.14084	0.75681	1047	3.396E-13	7.9E-15	1.783E-12	6.2E-14	2.501E+06	6.0E+04	1.456E+07	6.7E+05
Blank Batch A	A	B1464	A0514		0.14011	0.75207	708	1.31E-15	2.7E-16	3.9E-15	3.5E-15				
Blank Batch B	B	B1471	A0521		0.14011	0.75556	712	2.31E-15	4.7E-16	8.9E-15	4.8E-15				

[1] ^{9}Be carrier concentration was 2246 ± 11 µg/g for all samples

[2] ^{27}Al carrier concentration was 1000.5 ± 2.0 µg/mL, density = 1.011 g/cm^{3} for all samples

[3] ^{10}Be/^{9}Be ratios were normalized to SMD-Be-12, which has been cross calibrated to the NIST SRM 4325 standard (Akhmaldaliev et al., 2013; Nishiizumi et al., 2007).

[4] ^{26}Al/^{27}Al ratios were normalized to SMD-Al-11, which is traceable to primary standards MB04-A, MB04-B, and MB04-D (Rugel et al., 2016; Merchel and Bremser, 2004).

Table A2: Cl data from feldspar

Sample Name	Batch	DREAMS Cl Name	Feldspar Mass	^{35}Cl Carrier Solution Added[1]	Measured ^{36}Cl/^{35}Cl ratio[2]	^{36}Cl/^{35}Cl ratio unc.	Measured ^{35}Cl/^{37}Cl ratio	^{35}Cl/^{37}Cl ratio unc.	^{36}Cl	^{36}Cl unc. (1σ)	^{35}Cl + ^{37}Cl	^{35}Cl + ^{37}Cl unc. (1σ)
			g	g		1σ		1σ	atoms/g	atoms/g	μg/g	μg/g
LL030215-01	B	C0609	8.00462	0.99155	1.392E-12	3.0E-14	167.97	0.73	4.490E+06	9.6.E+04	3.038	0.056
LL030215-02A	A	C0602	9.53721	0.99372	1.155E-12	2.5E-14	102.6	1.0	3.173E+06	7.0.E+04	5.204	0.072
LL030215-02B	A	C0603	7.61495	0.99318	5.82E-13	1.4E-14	101.53	0.57	1.993E+06	4.9.E+04	6.599	0.066
LL030215-02C	A	C0604	8.61710	0.99175	6.88E-13	1.6E-14	79.37	0.45	2.100E+06	5.0.E+04	7.943	0.066
LL030215-03A	B	C0610	4.08165	0.99070	6.35E-13	1.5E-14	100.90	0.24	4.037E+06	9.8.E+04	12.25	0.10
LL030215-03B	B	C0611	13.19656	0.98943	2.000E-12	4.1E-14	32.71	0.10	4.243E+06	8.8.E+04	14.816	0.054
LL030215-03D	B	C0612	1.73175	0.99169	5.94E-13	1.4E-14	187.13	0.93	8.77E+06	2.2.E+05	11.79	0.24
LL030215-03E	B	C0613	3.14748	0.99187	1.392E-12	3.0E-14	118.01	0.33	1.151E+07	2.5.E+05	12.92	0.13
LL032215-01A	A	C0605	9.79858	0.99301	1.201E-12	2.6E-14	52.24	0.17	3.309E+06	7.1.E+04	11.577	0.056
LL032215-01B	A	C0606	10.07625	0.99075	1.043E-12	2.3E-14	47.12	0.14	2.806E+06	6.3.E+04	12.685	0.054
LL032215-01C	A	C0607	4.32011	0.99020	4.19E-13	1.1E-14	147.29	0.77	2.487E+06	6.7.E+04	6.978	0.099
Blank Batch A	A	C0601		0.99135	5.94E-15	9.6E-16	489	29				
Blank Batch B	B	C0608		0.99195	7.9E-15	1.1E-15	471	29				

Table A3: Feldspar, Quartz, and Pyroxene Compositions

Feldspar

Sample Name	K_2O %	CaO %	TiO_2 %	Fe_2O_3 %	Cl µg/g
LL030215-01	0.77	7.0	0.005	0.10	3.04
LL030215-02A	0.57	5.5	0.007	0.086	5.20
LL030215-02B	0.70	7.0	0.005	0.11	6.60
LL030215-02C	0.65	6.8	0.006	0.11	7.94
LL030215-03A	0.60	7.0	0.006	0.18	12.3
LL030215-03B	0.57	6.6	0.008	0.18	14.8
LL030215-03D	0.61	7.1	0.006	0.18	11.8
LL030215-03E	0.59	7.0	0.006	0.18	12.9
LL032215-01A	1.4	6.4	0.006	0.15	11.6
LL032215-01B	0.88	6.4	0.007	0.15	12.7
LL032215-01C	1.2	6.7	0.006	0.16	6.98

Quartz

Sample Name	U µg/g	Th µg/g
LL030215-01	0.044	0.13
LL030215-02A	0.11	0.068
LL030215-02B	0.052	0.10
LL030215-02C	0.035	0.067
LL030215-03A	0.0054	0.024
LL030215-03B	0.0056	0.031
LL030215-03D	0.0027	0.0088
LL030215-03E	0.0035	0.017
LL032215-01A	0.010	0.044
LL032215-01B	0.012	0.068
LL032215-01C	0.010	0.069

Pyroxene

Sample Name	CaO %	Fe_2O_3 %	MgO %	MnO %	Al_2O_3 %	Na_2O %	TiO_2 %	K_2O %	SiO_2* %	U µg/g	Th µg/g	Li µg/g
LL030215-02B	1.3	13	29	0.20	2.8	< 0.1	0.18	< 1	54	0.17	13	29
LL030215-02C	1.9	13	29	0.21	2.8	< 0.1	0.20	< 1	53	0.015	0.092	24
LL030215-03A	1.2	11	30	0.17	2.5	< 0.1	0.20	< 1	55	0.0086	0.025	45
LL030215-03B	1.5	15	38	0.23	3.1	< 0.1	0.26	< 1	42	0.0082	0.022	71
LL030215-03D	1.3	10	32	0.17	2.7	0.12	0.21	< 1	53	0.10	0.35	25
LL030215-03E	1.3	10	33	0.17	2.4	< 0.1	0.19	< 1	53	0.0062	0.009	25
LL030115-01B	1.5	25	26	1.0	1.6	< 0.1	0.35	< 1	45	0.052	0.28	22

For the feldspar samples, all elements were measured by ICP-OES except Cl, which was measured by isotope dilution accelerator mass spectrometry.

For the pyroxene samples, U, Th, and Li were measured by ICP-MS, the other elements were measured by ICP-OES.
* SiO_2 was not measured by ICP-OES, and thus was estimated by subtracting the sum of weight percent oxides of the other major elements from 100

Table A4: Whole rock sample compositions

Major Elements

Sample Name	H_2O	CO_2	Na_2O	MgO	Al_2O_3	SiO_2	P_2O_5	K_2O	CaO	TiO_2	MnO	Fe_2O_3
	%	%	%	%	%	%	%	%	%	%	%	%
LL030215-01*	1.2	0.050	3.1	0.57	16	67	0.28	4.1	3.1	0.76	0.045	3.4
LL030215-02A	1.5	0.090	3.0	2.4	16	63	0.32	3.4	4.4	0.74	0.079	4.9
LL030215-02B	1.4	0.060	2.9	2.5	16	63	0.32	3.4	4.3	0.78	0.083	5.2
LL030215-02C	1.3	0.060	3.0	2.2	16	64	0.27	3.2	4.3	0.69	0.063	4.5
LL030215-03A*	1.1	0.040	3.0	3.3	15	63	0.31	3.2	4.3	0.94	0.074	5.5
LL030215-03B	0.77	0.060	3.2	3.2	16	62	0.30	3.0	4.5	0.90	0.068	5.3
LL030215-03D	1.2	0.14	3.2	3.9	15	61	0.29	2.9	5.0	0.92	0.074	5.5
LL030215-03E	1.2	0.11	3.0	3.8	15	62	0.44	2.8	4.8	0.90	0.074	5.4
LL032215-01A	2.1	0.060	3.0	0.99	15	68	0.17	4.2	2.3	0.49	0.033	2.7
LL032215-01B	1.8	0.050	2.9	1.4	14	68	0.20	4.1	3.1	0.53	0.047	3.1
LL032215-01C*	1.8	0.060	2.8	1.4	15	68	0.18	4.5	2.4	0.55	0.038	3.1

Trace Elements

Sample Name	Cl	B**	Sm	Gd	U	Th	Cr	Li	Ba	Cr	Ga	Nb	Ni	Rb	Sr	V	Y	Zn	Zr
	µg/g	µg/g	µg/g	µg/g	µg/g	µg/g	µg/g	µg/g	µg/g	µg/g	µg/g	µg/g	µg/g	µg/g	µg/g	µg/g	µg/g	µg/g	µg/g
LL030215-01*	587	*37*	7.8	5.4	4.5	20	23	6.0	818	23	24	16	13	193	400	89	21	86	224
LL030215-02A	961	37	7.0	5.2	4.4	16	63	17	760	63	21	17	17	149	523	103	22	84	187
LL030215-02B	592	34	6.9	5.1	4.4	16	75	17	673	75	23	19	29	151	496	113	22	97	180
LL030215-02C	407	*34*	6.9	5.2	4.3	15	57	22	630	57	22	15	20	136	492	101	25	84	184
LL030215-03A*	615	44	7.2	5.3	4.6	16	108	30	710	108	20	16	48	131	437	130	21	89	196
LL030215-03B	474	*32*	6.9	5.2	4.1	14	108	44	675	108	22	13	41	112	475	120	20	83	192
LL030215-03D	654	*32*	7.4	5.6	4.0	13	163	25	632	163	24	12	43	119	430	141	22	97	180
LL030215-03E	665	32	6.3	4.7	4.0	13	153	20	570	153	20	13	38	120	420	129	17	88	180
LL032215-01A	612	39	7.4	4.5	9.3	31	21	38	573	21	27	10	<10	266	271	53	16	76	178
LL032215-01B	352	*39*	7.6	5.0	9.9	30	34	52	605	34	26	10	10	254	309	61	14	73	173
LL032215-01C*	1054	*39*	7.5	4.6	9.7	31	34	50	615	34	26	10	<10	269	281	65	16	81	182
LL022815-04A					2.0	7.4		16											
LL022815-04B					1.5	5.7		22											
LL030115-01B					2.4	10		15											
LL030115-01C					2.3	10		16											

* Whole rock sample was unavailable, thus >1000 µm fraction was measured

** B was measured for LL030215-02A, LL030215-02B, LL030215-03A, LL030215-03E, and LL032215-01A. For the other samples, a value from a rock of similar lithology was used, shown in italics

Table A5: Ne data from quartz

Sample Name	Mass	Run	Temp	^{20}Ne	1σ	^{22}Ne/^{20}Ne	1σ	^{21}Ne/^{20}Ne	1σ	^{21}Ne$_{ex}$	1σ
	g		°C	10^8 at/g	10^8 at/g	10^{-3}	10^{-3}	10^{-3}	10^{-3}	10^6 at/g	10^6 at/g
LL030215-02C	1.00222		Crush	6.75	0.18	101.62	0.93	3.013	0.08862		
LL030215-02A	1.01414		Crush	5.31	0.14	102.14	0.94	3.075	0.09394		
LL032215-01C	1.00190		Crush	2.352	0.065	101.6	1.0	3.02	0.24		
LL030215-01	0.70424	2	400	8.88	0.24	119.78	0.70	17.97	0.20	13.26	0.38
			800	6.84	0.21	118.3	1.4	16.52	0.31	9.22	0.31
			Total							**22.49**	**0.49**
LL030215-02A	0.70532	2	400	6.63	0.19	110.17	0.52	8.95	0.22	3.91	0.18
			800	10.28	0.29	119.50	0.47	16.98	0.18	14.33	0.40
			Total							**18.25**	**0.44**
LL030215-02B	0.70396	2	400	10.77	0.30	111.13	0.88	10.26	0.15	7.78	0.27
			800	5.29	0.17	103.4	1.3	4.40	0.13	0.72	0.07
			Total							**8.50**	**0.28**
LL030215-02C	0.70544	1	400	5.86	0.20	107.1	1.1	6.82	0.28	2.21	0.18
			800	9.22	0.32	113.29	0.69	11.79	0.24	8.06	0.33
			Total							**10.27**	**0.37**
LL030215-03A	0.70354	1	400	11.04	0.36	121.72	0.78	18.32	0.24	16.86	0.58
			800	3.49	0.16	115.3	1.2	15.41	0.60	4.31	0.22
			Total							**21.17**	**0.62**
LL030215-03B	0.70598	1	400	10.90	0.35	125.80	0.84	21.83	0.23	20.49	0.68
			800	4.62	0.19	116.5	1.7	15.19	0.35	5.62	0.21
			Total							**26.11**	**0.71**
LL030215-03D	0.70294	2	400	7.17	0.20	121.84	0.61	19.81	0.32	12.02	0.38
			800	5.20	0.17	170.0	1.3	61.3	1.2	30.31	0.90
			Total							**42.33**	**0.97**
LL030215-03E	0.70508	2	400	9.22	0.25	152.78	0.83	45.43	0.52	39.1	1.1
			800	2.89	0.12	214.3	4.0	99.4	2.7	27.85	0.78
			Total							**66.9**	**1.3**
LL032215-01A	0.70288	2	400	11.63	0.32	111.87	0.54	9.82	0.12	7.89	0.26
			800	3.79	0.14	117.37	0.82	18.48	0.54	5.86	0.23
			Total							**13.74**	**0.34**
LL032215-01B	0.70316	1	400	9.68	0.32	111.59	0.77	9.90	0.29	6.64	0.36
			800	3.70	0.16	121.9	1.7	19.12	0.65	5.96	0.26
			Total							**12.60**	**0.44**
LL032215-01C	0.70262	2	400	11.57	0.31	110.34	0.68	8.90	0.13	6.78	0.24
			800	2.57	0.11	122.9	1.8	22.01	0.70	4.88	0.17
			Total							**11.67**	**0.29**
For reference:											
CREU-1	0.10326	1	400	5.76	0.45	251	15	137	10	77.1	3.1
			800	159.3	4.3	116.83	0.51	17.24	0.17	227.4	6.5
			1200	124.5	3.3	105.87	0.45	6.47	0.11	43.7	1.8
			Total							**348.2**	**7.4**
CREU-1	0.10172	2	400	7.27	0.47	209.4	6.5	101.8	5.6	71.9	2.2
			800	173.3	4.6	116.68	0.75	16.22	0.15	229.8	6.4
			1200	138.9	3.6	105.52	0.38	6.258	0.067	45.8	1.5
			Total							**347.5**	**6.9**

Sample ^{21}Ne excesses (^{21}Ne$_{ex}$) calculated assuming a trapped ^{21}Ne/^{20}Ne ratio of 0.00304 +/- 0.00013, which is the error-weighted mean of three crushing extractions: LL030215-02A, LL030215-02C, LL032215-01C

CREU-1 ^{21}Ne excesses were calculated assuming an atmospheric trapped ^{21}Ne/^{20}Ne ratio of 0.002959

Table A6: He and Ne data from pyroxene

Sample Name	Mass	Temp	^{4}He	1σ	^{3}He	1σ	^{3}He/^{4}He	1σ	^{3}He$_{Sp}$	1σ[1]	^{20}Ne	1σ	^{22}Ne/^{20}Ne	1σ	^{21}Ne/^{20}Ne	1σ	^{21}Ne$_{ex}$[2]	1σ
	g	°C	10^{11} at/g	10^{11} at/g	10^{6} at/g	10^{6} at/g	10^{-6}	10^{-6}	10^{6} at/g	10^{6} at/g	10^{8} at/g	10^{8} at/g	10^{-3}	10^{-3}	10^{-3}	10^{-3}	10^{6} at/g	10^{6} at/g
LL030215-02B	0.50936	Crush	5.01	0.10	0.161	0.015	0.321	0.029			1.393	0.035	101.87	0.80	3.046	0.065		
LL030215-02C	0.56818	Crush	0.659	0.019	0.303	0.016	4.60	####			9.37	0.22	101.58	0.70	2.992	0.074		
LL030215-03A	0.57330	Crush	0.9558	0.0029	0.389	0.025	4.07	####										
LL030215-03B	0.52280	Crush	0.142	0.013	0.194	0.012	13.68	####			1.369	0.043	102.8	1.2	3.037	0.073		
LL030215-03D	0.56682	Crush	0.1389	0.0028	0.354	0.017	25.5	1.1			20.96	0.47	102.35	####	2.975	0.052		
LL030215-03E	0.47324	Crush	0.05188	0.0014	0.429	0.036	82.6	6.6			1.497	0.037	102.7	1.2	3.23	0.10		
LL030115-01B	0.54268	Crush	0.2490	0.0051	1.191	0.053	47.8	####			2.340	0.054	102.9	1.3	3.33	####		
LL030215-02B	0.27794	900	173.0	3.5	54.5	1.2	3.151	0.033			3.316	0.080	103.05	0.72	4.31	0.12	0.448	0.017
		1750	54.1	1.1	19.92	0.48	3.681	0.051			20.44	0.45	111.29	0.87	11.40	0.14	17.26	0.44
		Total			**74.4**	**1.3**			**69.0**	**1.3**							**17.70**	**0.44**
LL030215-02C	0.35916	900	106.1	2.1	64.8	1.4	6.107	0.057			5.62	0.12	102.48	0.81	5.02	0.10	1.161	0.035
		1750	11.10	0.22	21.58	0.51	19.43	0.24			5.56	0.12	132.20	0.94	37.32	0.54	19.09	0.49
		Total			**86.4**	**1.5**			**81.2**	**1.5**							**20.25**	**0.49**
LL030215-03A	0.29914	900	74.3	1.5	149.5	3.2	20.12	0.14			3.942	0.091	113.46	0.68	14.51	0.39	4.55	0.16
>100 µm		1750	10.36	0.21	47.4	1.1	45.80	0.47			5.32	0.12	173.3	1.7	75.05	0.74	38.32	0.94
		Total			**196.9**	**3.3**			**180.5**	**3.3**							**42.9**	**1.0**
LL030215-03A	0.20806	900	84.9	1.7	191.0	4.2	22.49	0.20			5.32	0.12	128.7	1.4	31.58	0.69	15.23	0.48
<100 µm		1750	1.779	0.037	5.85	0.17	32.89	0.71			4.40	0.10	161.2	5.1	65.9	1.4	27.71	0.87
		Total			**196.8**	**4.2**											**42.9**	**1.0**
LL030215-03B	0.32822	900	109.1	2.2	181.5	3.9	16.63	0.14			4.431	0.094	115.6	1.1	17.07	0.47	6.25	0.22
		1750	12.24	0.25	55.1	1.3	45.01	0.51			4.65	0.10	189.5	3.8	95.6	1.5	43.1	1.2
		Total			**236.6**	**4.1**			**204.7**	**4.1**							**49.4**	**1.2**
LL030215-03D	0.35348	900	56.0	1.1	284.8	6.1	50.82	0.41			11.67	0.24	108.36	0.71	9.64	0.14	7.80	0.20
		1750	5.72	0.12	90.3	2.0	158.0	1.5			9.33	0.20	192.9	1.6	90.5	1.2	81.7	2.0
		Total			**375.1**	**6.5**			**352.2**	**6.5**							**89.5**	**2.1**
LL030215-03E	0.29826	900	32.96	0.66	423.1	9.2	128.4	1.1			3.577	0.084	128.4	1.4	31.27	0.69	10.13	0.33
		1750	3.456	0.070	125.1	2.8	361.9	3.3			4.266	0.091	407.6	4.5	303.2	4.1	128.1	3.2
		Total			**548.2**	**9.6**			**511.7**	**9.6**							**138.2**	**3.3**
LL022815-04A	0.18706	900	344.4	6.9	60.2	1.4	1.747	0.022			5.25	0.12	112.2	2.3	15.09	0.42	6.37	0.23
		1750	80.3	1.6	4.61	0.18	0.574	0.019			4.51	0.10	114.8	1.8	21.86	0.67	8.53	0.33
		Total			**64.8**	**1.4**			**59.6**	**1.4**							**14.89**	**0.40**
LL022815-04B	0.14620	900	50.4	1.0	400.9	8.7	79.48	0.69			5.44	0.13	143.5	3.6	46.7	1.3	23.83	0.86
		1750	8.96	0.18	107.6	2.7	120.0	1.7			5.42	0.12	248.9	5.2	156.5	3.8	83.1	2.7
		Total			**508.5**	**9.1**			**469.4**	**9.1**							**107.0**	**2.8**
LL030115-01B	0.30830	900	64.3	1.3	506	11	78.73	0.65			4.57	0.10	162.8	2.4	65.10	0.96	28.42	0.76
		1750	10.68	0.21	116.0	2.6	108.6	1.0			4.311	0.094	331.5	5.0	231.1	3.2	98.4	2.5
		Total			**622**	**11**			**574**	**11**							**126.8**	**2.7**
LL030115-01C	0.05826	900	49.07	0.98	193.4	4.2	39.41	0.34			17.51	0.42	111.3	1.8	12.12	0.35	16.04	0.60
		1750	6.56	0.13	27.88	0.92	42.5	1.1			13.63	0.30	122.9	2.3	24.48	0.68	29.3	1.0
		Total			**221.2**	**4.3**			**204.2**	**4.3**							**45.4**	**1.2**
For reference:																		
CRONUS P	0.04980	900	337.5	6.8	4819	100	142.80	0.83			24.02	0.56	208.7	2.8	107.9	2.0	252.1	7.5
		1750	2.346	0.079	45.0	1.3	191.9	6.0			27.09	0.63	460.2	8.9	343.7	4.6	923	25
		Total			**4860**	**100**											**1175**	**26**
CRONUS P	0.05038	900	327.4	6.5	4740	100	144.8	1.2			20.69	0.44	233.1	4.6	126.7	1.9	256.0	6.7
		1750	3.057	0.070	47.2	1.2	154.5	2.9			25.02	0.53	500.2	9.4	380.6	4.2	945	23
		Total			**4790**	**100**											**1201**	**24**

[1] Uncertainty on spallation produced 3He is assumed to be the same as the analytical uncertainty, as it is difficult to assess the uncertainty associated with the thermal neutron produced ^{3}He concentration. This may be a slight underestimation.

[2] Sample ^{21}Ne excesses (^{21}Ne$_{ex}$) calculated assuming a trapped ^{21}Ne/^{20}Ne ratio of 0.002959

Table A7: Corrections for radiogenic ^{4}He and thermal neutron produced ^{3}He

Sample Name	U*	Th*	Li**	Total ^{3}He	Total ^{3}He unc. (1σ)	cosmogenic thermal neutron prod. ^{3}He[1]	nucleogenic thermal neutron prod. ^{3}He[2]	total thermal neutron prod. ^{3}He	% of measured ^{3}He thermal neutron prod.	spallation produced ^{3}He	spallation produced ^{3}He unc. (1σ)[3]	% of measured ^{3}He spallation produced	measured ^{4}He	calculated radiogenic ^{4}He[2,4]	% of measured ^{4}He calculated radiogenic
	μg/g	μg/g	μg/g	10^6 at/g	10^6 at/g	10^6 at/g	10^6 at/g	10^6 at/g		10^6 at/g	10^6 at/g		10^{11} at/g	10^{11} at/g	
LL030215-02B	0.17	13	29	74.4	1.3	3.0	2.5	5.4	7%	69.0	1.3	93%	227	974	429%
LL030215-02C	0.015	0.092	24	86.4	1.5	3.1	2.1	5.2	6%	81.2	1.5	94%	117	211	180%
LL030215-03A	0.0086	0.025	45	196.9	3.3	12.8	3.6	16	8%	180.5	3.3	92%	84.6	221	261%
LL030215-03B	0.0082	0.022	71	236.6	4.1	26.3	5.6	32	13%	204.7	4.1	87%	121	196	161%
LL030215-03D	0.10	0.35	25	375.1	6.5	21.0	1.9	23	6%	352.2	6.5	94%	61.7	226	367%
LL030215-03E	0.0062	0.0088	25	548	10	34.6	1.9	37	7%	512	10	93%	36.4	187	512%
LL022815-04A	*0.052*	*0.28*	*22*	64.8	1.4	4.0	1.2	5.2	8%	59.6	1.4	92%	425	125	29%
LL022815-04B	*0.052*	*0.28*	*22*	508.5	9.1	38.1	0.9	39.1	8%	469.4	9.1	92%	59.4	101	171%
LL030115-01B	0.052	0.28	*22*	622	11	46.8	1.6	48.3	8%	574	11	92%	75.0	151	202%
LL030115-01C	*0.052*	*0.28*	*22*	221.2	4.3	15.5	1.6	17.0	8%	204.2	4.3	92%	55.6	149	267%

[1] cosmogenic thermal neutron component calculated using the sample's ^{10}Be exposure age and assuming 1 mm/kyr erosion

[2] nucleogenic thermal neutron and radiogenic ^{4}He production calculated assuming a closure age of 8 Myr

[3] Uncertainty on spallation produced ^{3}He is assumed to be the same as the analytical uncertainty, as it is difficult to assess the uncertainty associated with the thermal neutron produced ^{3}He concentration. This may be a slight underestimation.

[4] Radiogenic ^{4}He was calculated following Blard and Farley (2008) and assuming a pyroxene diameter of 300 μm.
Calculated radiogenic ^{4}He values higher than measured can be explained by the fact that some pyroxene material was removed during chemical leaching

* U and Th were not measured in pyroxene separates for samples LL022815-04A, LL022815-04B, and LL030115-01C
The U and Th concentrations of LL030115-01B were used instead

Table A8: Decay and erosion corrected production ratios with 1σ uncertainties

Sample Name	^{3}He/^{10}Be	^{3}He/^{10}Be unc.	^{3}He/^{21}Ne$_{qtz}$	^{3}He/^{21}Ne$_{qtz}$ unc.	^{3}He/ ^{21}Ne$_{px}$	^{3}He/^{21}Ne$_{px}$ unc.	^{3}He/^{26}Al	^{3}He/^{26}Al unc.	^{10}Be/^{21}Ne$_{qtz}$	^{10}Be/^{21}Ne$_{qtz}$ unc.	^{10}Be/^{21}Ne$_{px}$	^{10}Be/^{21}Ne$_{px}$ unc.	^{26}Al/^{10}Be	^{26}Al/^{10}Be unc.	^{21}Ne$_{qtz}$/ ^{21}Ne$_{px}$	^{21}Ne$_{qtz}$/^{21}Ne$_{px}$ unc.	^{21}Ne$_{qtz}$/^{26}Al	^{21}Ne$_{qtz}$/^{26}Al unc.	^{21}Ne$_{px}$/^{26}Al	^{21}Ne$_{px}$/^{26}Al unc.
LL030215-01									0.2345	0.0081			6.06	0.29			0.704	0.032		
LL030215-02A									0.2263	0.0074			5.42	0.23			0.816	0.036		
LL030215-02B	35.3	1.0	8.13	0.31	3.90	0.12	6.09	0.28	0.2304	0.0090	0.1105	0.0037	5.79	0.28	0.480	0.020	0.749	0.040	1.562	0.077
LL030215-02C	37.7	1.1	7.91	0.32	4.01	0.12	6.30	0.28	0.2101	0.0089	0.1064	0.0035	5.98	0.27	0.507	0.022	0.796	0.043	1.572	0.073
LL030215-03A	38.1	1.2	8.51	0.29	4.21	0.12	6.47	0.28	0.2234	0.0083	0.1104	0.0036	5.89	0.27	0.494	0.018	0.760	0.037	1.537	0.070
LL030215-03B	37.1	1.1	7.84	0.26	4.15	0.13	6.19	0.26	0.2113	0.0072	0.1117	0.0036	6.00	0.25	0.529	0.019	0.789	0.036	1.492	0.066
LL030215-03C													5.86	0.26						
LL030215-03D*	33.6	0.9	8.33	0.24	3.94	0.12	5.70	0.24	0.2479	0.0076	0.1172	0.0036	5.89	0.25	0.473	0.015	0.685	0.030	1.449	0.063
LL030215-03E*	31.5	0.9	7.65	0.21	3.70	0.11	4.89	0.20	0.2429	0.0070	0.1176	0.0037	6.44	0.27	0.484	0.015	0.639	0.027	1.321	0.057
LL032215-01A									0.218	0.026			4.61	1.26			1.00	0.25		
LL032215-01B									0.2309	0.0094			6.20	0.28			0.698	0.037		
LL032215-01C									0.2164	0.0075			5.88	0.30			0.787	0.041		
Error weighted mean, 1σ weighted standard deviation																				
	37.0	**1.1**	**8.09**	**0.27**	**4.06**	**0.12**	**6.26**	**0.14**	**0.2222**	**0.0086**	**0.1097**	**0.0020**	**5.87**	**0.24**	**0.502**	**0.018**	**0.759**	**0.044**	**1.538**	**0.032**

Supplementary Boulder Library

LL032215 - 01A

Moraine: Quevar
Latitude, Longitude: -24.35500°, -66.78946°
Elevation (masl): 4990

^{10}Be age: 45.9 ± 6.0 ka

LL032215 - 01B

Moraine: Quevar
Latitude, Longitude: -24.35516°, -66.78952°
Elevation (masl): 4987

^{10}Be age: 45.6 ± 1.7 ka

LL032215 - 01C

Moraine: Quevar
Latitude, Longitude: -24.35528°, -66.78972°
Elevation (masl): 4981

^{10}Be age: 38.9 ± 1.3 ka

LL030215 - 02A

Moraine: Quiron M2
Latitude, Longitude: -24.41263°, -66.80383°
Elevation (masl): 4610

^{10}**Be age:** 75.5 ± 3.2 ka

LL030215 - 02B

Moraine: Quiron M2
Latitude, Longitude: -24.41265°, -66.80392°
Elevation (masl): 4604

^{10}**Be age:** 41.5 ± 1.2 ka

LL030215 - 02C

Moraine: Quiron M2
Latitude, Longitude: -24.41275°, -66.80386°
Elevation (masl): 4602

^{10}**Be age:** 39.2 ± 1.2 ka

LL030215 - 03A

Moraine: Quiron M1
Latitude, Longitude: -24.41544°, -66.80778°
Elevation (masl): 4511

^{10}Be age: 96.8 ± 3.5 ka

LL030215 - 03B

Moraine: Quiron M1
Latitude, Longitude: -24.41563°, -66.80794°
Elevation (masl): 4505

^{10}Be age: 110.2 ± 3.9 ka

LL030215 - 03C

Moraine: Quiron M1
Latitude, Longitude: -24.41574°, -66.80800°
Elevation (masl): 4509

^{10}Be age: 197.8 ± 8.1 ka

LL030215 - 03D

Moraine: Quiron M1
Latitude, Longitude: -24.41631°, -66.80800°
Elevation (masl): 4480

^{10}Be age: 227 ± 12 ka

LL030215 - 03E

Moraine: Quiron M1
Latitude, Longitude: -24.41708°, -66.80934°
Elevation (masl): 4474

^{10}Be age: 392 ± 22 ka

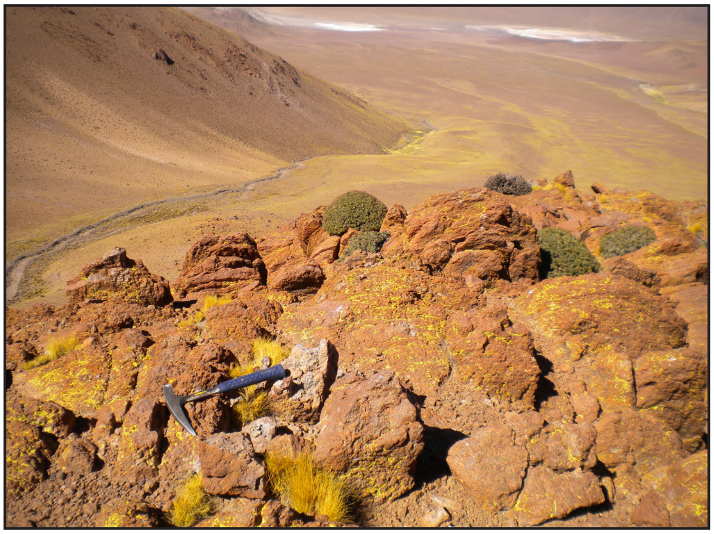

LL030215 - 01

Moraine: Quiron M1
Latitude, Longitude: -24.41061°, -66.80299°
Elevation (masl): 4695

^{10}Be age: 95.7 ± 3.7 ka

LL022815 - 04A

Moraine: Pocitos
Latitude, Longitude: -24.28051°, -66.99042°
Elevation (masl): 4136

^{3}He age: 44.1 ± 2.1 ka

LL022815 - 04B

Moraine: Pocitos
Latitude, Longitude: -24.28041°, -66.99028°
Elevation (masl): 4135

^{3}He age: 498 ± 37 ka

LL030115 - 01B

Moraine: Del Medio
Latitude, Longitude: -24.23990°, -67.06596°
Elevation (masl): 3993

^{3}He age: 800 ± 59 ka

LL030115 - 01C

Moraine: Del Medio
Latitude, Longitude: -24.23991°, -67.06608°
Elevation (masl): 3997

^{3}He age: 175 ± 11 ka